

# Shock finding on a moving-mesh: II. Hydrodynamic shocks in the Illustris universe

Kevin Schaal<sup>1,2\*</sup>, Volker Springel<sup>1,2</sup>, Rüdiger Pakmor<sup>1</sup>, Christoph Pfrommer<sup>1</sup>, Dylan Nelson<sup>3</sup>, Mark Vogelsberger<sup>4</sup>, Shy Genel<sup>5†</sup>, Annalisa Pillepich<sup>6</sup>, Debora Sijacki<sup>7</sup>, Lars Hernquist<sup>6</sup>

<sup>1</sup>Heidelberg Institute for Theoretical Studies, Schloss-Wolfsbrunnengasse 35, D-69118 Heidelberg, Germany

<sup>2</sup>Zentrum für Astronomie der Universität Heidelberg, Astronomisches Recheninstitut, Mönchhofstr. 12-14, 69120 Heidelberg, Germany

<sup>3</sup>Max-Planck-Institut für Astrophysik, Karl-Schwarzschild-Straße 1, 85740 Garching bei München, Germany

<sup>4</sup>Department of Physics, Kavli Institute for Astrophysics & Space Research, MIT, Cambridge, MA 02139, USA

<sup>5</sup>Department of Astronomy, Columbia University, 550 West 120th Street, New York, NY 10027, USA

<sup>6</sup>Harvard-Smithsonian Center for Astrophysics, 60 Garden Street, Cambridge, MA 02138, USA

<sup>7</sup>Institute of Astronomy and Kavli Institute for Cosmology, University of Cambridge, Madingley Road, Cambridge CB3 0HA, UK

Published: 4.7.2016

## ABSTRACT

Hydrodynamical shocks are a manifestation of the non-linearity of the Euler equations and play a fundamental role in cosmological gas dynamics. In this work, we identify and analyse shocks in the Illustris simulation, and contrast the results with those of non-radiative runs. We show that simulations with more comprehensive physical models of galaxy formation pose new challenges for shock finding algorithms due to radiative cooling and star-forming processes, prompting us to develop a number of methodology improvements. We find in Illustris a total shock surface area which is about 1.4 times larger at the present epoch compared to non-radiative runs, and an energy dissipation rate at shocks which is higher by a factor of around 7. Remarkably, shocks with Mach numbers above and below  $\mathcal{M} \approx 10$  contribute about equally to the total dissipation across cosmic time. This is in sharp contrast to non-radiative simulations, and we demonstrate that a large part of the difference arises due to strong black hole radio-mode feedback in Illustris. We also provide an overview of the large diversity of shock morphologies, which includes complex networks of halo-internal shocks, shocks on to cosmic sheets, feedback shocks due to black holes and galactic winds, as well as ubiquitous accretion shocks. In high redshift systems more massive than  $10^{12} M_{\odot}$  we discover the existence of a double accretion shock pattern in haloes. They are created when gas streams along filaments without being shocked at the outer accretion shock, but then forms a second, roughly spherical accretion shock further inside.

**Key words:** hydrodynamics – shock waves – methods: numerical – galaxies: clusters: general – galaxies: kinematics and dynamics – large-scale structure of Universe

## 1 INTRODUCTION

Hydrodynamical shock waves play an important role in the evolution of the baryonic component of our Universe. During the process of hierarchical structure formation, shocks dissipate and thermalize kinetic energy in supersonic gas flows, thereby heating the cosmic web and structures therein. Gas inside dark matter haloes can be compressed and virialized by means of shocks, before radiative cooling in the densest regions allows it to collapse further, eventually leading to the formation of stars and accretion on to black holes (BHs). Supersonic gas motions are also created by feedback

processes such as stellar winds, supernovae (SNe) explosions, or relativistic jets from active galactic nuclei (AGN). The conversion of the released mechanical energy to thermal energy in the ambient gas is again mediated by thermalization processes that ultimately involve hydrodynamical shocks.

Unlike in classical hydrodynamical shocks in which the kinetic energy of a fluid is thermalized via particle collisions, shocks on cosmological and galactic scales are *collisionless*. This is because the mean free path of particles in the corresponding environments is large compared to the transition layer between the pre-shock and post-shock regions. In this case, the energy transfer is mediated by electromagnetic viscosity (Wentzel 1974; Kennel et al. 1985). Interestingly, collisionless shocks are also sites of diffusive shock ac-

\* e-mail: kevin.schaal@h-its.org

† Hubble Fellow

celeration (DSA; Axford et al. 1977; Krymskii 1977; Bell 1978a,b; Blandford & Ostriker 1978; Malkov & O’C Drury 2001), creating relativistic cosmic rays. In this process, ions inside the converging flow can cross the shock multiple times by scattering off the magnetic field fluctuations in the pre- and post-shock regions, thereby gaining more and more energy with every crossing. The net result is a power law momentum spectrum of energetic particles, thus creating a non-thermal cosmic ray particle component that may modify the gas dynamics in important ways. This in particular happens in SN remnants, but may also be important for accretion shocks around dark matter haloes and AGN.

Directly observing cosmological shocks is in general very difficult. While the central high density regions of galaxy clusters can be observed in X-ray, the gas temperature in these environments is high as well. This allows only for low Mach number shocks, and these are difficult to detect since the density contrast between the shocked and unshocked gas is small. Still, a number of bow shocks in merging clusters have been discovered by analysing *XMM-Newton* observations (e.g. Finoguenov et al. 2010; Ogorean et al. 2013a) and *Chandra* observations (e.g. Markevitch et al. 2005; Macario et al. 2011; Russell et al. 2014; Dasadia et al. 2016), the most famous being the Mach number  $\mathcal{M} \approx 3$  shock in the bullet cluster (Markevitch et al. 2002). Moreover, pressure jumps associated with shocks have been detected with the *Planck* space telescope at the outskirts of the Coma cluster (Planck Collaboration 2013; Erler et al. 2015).

Fortunately, the synchrotron emission of accelerated or reaccelerated electrons can reveal the location of a cosmological shock more easily. Relativistic cosmic ray electrons have short lifetimes, and their non-thermal emission is therefore confined to a region close to the accelerating shock. There is strong evidence that radio relics (e.g. Feretti 2005; Ferrari et al. 2008; Brüggén et al. 2011), which can be found in peripheral cluster regions, are associated with merger shocks (Ensslin et al. 1998; Miniati et al. 2001; Pfrommer et al. 2008; Pfrommer 2008; Pinzke et al. 2013; Skillman et al. 2013). These sources are elongated and often curved, with length-scales up to a few Mpc. Moreover, the emitted photons are highly polarized and indicate in many cases a magnetic field which is aligned with the relic (Brüggén et al. 2012). Strikingly, for a few clusters the associated shock is directly observed in the form of an X-ray edge (e.g. Markevitch 2010; Akamatsu & Kawahara 2013; Bourdin et al. 2013; Ogorean & Brüggén 2013; Owers et al. 2014).

On the other hand, for a few merging clusters the presence of X-ray surface brightness discontinuities does not correlate with observable radio emission, or the spectral index of the radio emission implies a Mach number which is inconsistent with the density jump detected in X-rays (e.g. Russell et al. 2011; Ogorean et al. 2013b, 2014). These cases may be influenced by projection effects, but they may also indicate that DSA directly from the thermal pool is not sufficient, in particular at weak shocks.

Radio relics are very interesting objects to study with the current generation of radio observatories, but they are in principle only the brightest components of a much larger entity, the magnetized cosmic web. The cosmic web consists of non-linear structures in the form of a network of filaments and nodes, which is expected to be surrounded by more or less stationary accretion shocks. Based on current estimates for the magnetisation and electron acceleration efficiencies at these shocks, the expected synchrotron radiation will be in reach of the Square Kilometre Array (SKA) (Keshet et al. 2004; Battaglia et al. 2009; Vazza et al. 2015). Consequently, in the near future it should become possible to observe filaments of the

cosmic web and their surrounding shocks, providing a novel probe of cosmic large-scale structure formation and the simultaneous opportunity to test simulation models.

In this paper, we analyse shock waves in an advanced cosmological simulation of galaxy formation, the Illustris Simulation. It is the second work in a short series on shocks in numerical hydrodynamic simulations. In our first paper (Schaal & Springel 2015), we have introduced our shock finding algorithm which operates on the Voronoi mesh of the AREPO code (Springel 2010), and analysed non-radiative cosmological simulations of gas and dark matter. Those simulations did not incorporate cooling or feedback of any kind, and hence the shocks which are present can mostly be classified as merger shocks and accretion shocks. In this case, the shock statistics features a bimodality where so-called external shocks enter with high Mach numbers and internal shocks inside structures with relatively low Mach numbers (Ryu et al. 2003). The external shocks are created when pristine gas accretes on to the cosmic web and gets shock heated for the first time. While the corresponding flows are highly supersonic, only a little kinetic energy is thermalized due to the low densities involved. On the other hand, internal flows are characterized by high temperatures and densities, which lead to very energetic low Mach number shocks.

Shocks in such non-radiative simulations have been analysed extensively in previous studies (see for example Quilis et al. (1998); Miniati et al. (2000); Ryu et al. (2003); Pfrommer et al. (2006); Skillman et al. (2008); Vazza et al. (2009a, 2010); Schaal & Springel (2015), and Vazza et al. (2011) for a code comparison project), but only few authors have explored runs including radiative physics and stellar feedback (e.g. Kang et al. 2007; Pfrommer et al. 2007; Planelles & Quilis 2013; Hong et al. 2014, 2015) or AGN feedback (Vazza et al. 2013, 2014). It is therefore the aim of our second paper in this series to investigate shocks in a state-of-the-art cosmological simulation that includes gas and dark matter, as well as stars and BHs and their associated feedback processes. These feedback sources are expected to create powerful additional shocks, making it particularly interesting to compare the resulting shock statistics with those obtained for the non-radiative runs. We shall use the Illustris simulation suite (Vogelsberger et al. 2014b,c; Genel et al. 2014) for our study, focusing on the highest-resolution, full physics run (Illustris-1), also known as *the* Illustris simulation. This is among the presently most successful simulations of galaxy formation and uses an accurate mesh-based hydrodynamical method, making it particularly well suited for our purposes.

The paper is structured as follows. Section 2 recaps the analysed simulations, the simulation technique, and the shock finding method. Section 3 focuses on the interpretation of shock statistics, both in a global sense and within different environments. In Section 4, we present shock morphologies across cosmic time and discuss what they can reveal about the gas dynamics. Variations in our shock finding techniques that test our methodology are investigated in Section 5, and our findings are summarized and discussed in Section 6. Lastly, we study resolution effects in Appendix A.

## 2 ANALYSING SHOCKS IN THE ILLUSTRIS UNIVERSE

### 2.1 The Illustris project

At the centre of the Illustris project is the cosmological hydrodynamical simulation Illustris-1 (Vogelsberger et al. 2014b,c; Genel et al. 2014). It evolves around  $1.2 \times 10^{10}$  resolution elements of dark matter and baryons in a comoving periodic volume  $75 h^{-1}$  Mpc on a

side. With this setup a dark matter mass resolution of  $6.26 \times 10^6 M_\odot$  and an initial gas mass resolution of  $1.26 \times 10^6 M_\odot$  are achieved. The simulations of the Illustris project adopt the standard  $\Lambda$  cold dark matter model and cosmological parameters according to the 9-year *Wilkinson Microwave Anisotropy Probe* (WMAP9) observations (Hinshaw et al. 2013), with the following values:  $\Omega_m = 0.2726$ ,  $\Omega_\Lambda = 0.7274$ ,  $\Omega_b = 0.0456$ ,  $\sigma_8 = 0.809$ ,  $n_s = 0.963$ , and  $H_0 = 100 h \text{ km s}^{-1} \text{ Mpc}^{-1}$  where  $h = 0.704$ .

The simulations of Illustris were carried out with the moving-mesh code AREPO (Springel 2010) and a galaxy formation physics implementation described and validated in detail in Vogelsberger et al. (2013) and Torrey et al. (2014). In the following, we briefly summarize the key features of the physics model adopted for Illustris-1. The interstellar medium (ISM) is represented through a sub-resolution approach with an effective equation of state following Springel & Hernquist (2003). In this model, a self-regulated ISM arises through the interplay of gas cooling, star formation, supernova (SN) feedback and galactic winds. Star particles are created stochastically in overdense regions according to the estimated local star formation rate, and represent single-age stellar populations characterized by a Chabrier (2003) initial mass function (IMF). Additionally, SNe energy is injected as purely kinetic energy of wind particles. The latter are briefly decoupled from the hydrodynamic scheme until they leave the dense star-forming region and can deposit their momentum into the surrounding lower density gas. Black holes (BHs) and the associated energy feedback processes from gas accretion are implemented following Springel et al. (2005) and Sijacki et al. (2007).

Collisionless BH sink particles are inserted at the potential minima of newly identified dark matter haloes that do not yet contain BHs. To be precise, a BH particle is seeded if the friends-of-friends group is more massive than  $5 \times 10^{10} h^{-1} M_\odot$ , and its initial mass is set to  $10^5 h^{-1} M_\odot$ . A repositioning scheme ensures that BH particles always stay in the minimum of their halo potential. They grow in mass by accretion and BH merger events. The accretion is parametrized by means of a Bondi-Hoyle-Lyttleton accretion rate (Hoyle & Lyttleton 1939; Bondi & Hoyle 1944; Bondi 1952), and limited by the Eddington rate. These rates are calculated with respect to the parent gas cell of a BH sink particle, and in every timestep mass is drained from this cell and transferred to the BH.

For high accretion rates relative to the Eddington rate, the BH is assumed to be in a quasar-mode, and the model couples the feedback energy thermally to the surrounding gas. For low accretion rates, a different feedback channel, a radio-mode, is assumed in which mechanical feedback occurs through jets. Since the jets cannot be directly resolved, the hot radio bubbles inflated by them are instead modelled through an injection of heat energy in spherical volumes corresponding to the bubbles. Additionally, a scheme for radiative AGN feedback is adopted in which the elevated ionizing flux and its impact on the cooling rates is accounted for in the proximity of actively accreting BHs. The total radiative heating rate of the gas is calculated by the superposition of the AGN radiation field and a spatially uniform but time-dependent photoionizing UVB (UVB). The cooling rate in the simulations has three contributions: atomic cooling based on the equations describing the ionization balance of hydrogen and helium (Katz et al. 1996), metal line cooling calculated from pre-computed cooling tables, and Compton cooling off the cosmic microwave background. Nine different elements are explicitly tracked in the simulation (H, He, C, N, O, Ne, Mg, Si, Fe), whose abundance is increased by stellar winds from AGB stars, core collapse SNe (SN), and type-Ia SNe.

With this setup of the Illustris simulations, a significant number

of basic properties of the galaxy population beyond those used in tuning the model (which are mostly the present-day stellar mass function and the cosmic star formation rate history) have been found to be in good agreement with observations. Remarkably, these include realistic morphologies and velocity structures for around 40000 well-resolved galaxies (Vogelsberger et al. 2014b,c; Genel et al. 2014; Snyder et al. 2015; Torrey et al. 2015). The simulation also contains 32552 BHs at  $z = 0$  with properties that match observed quasar luminosity functions and galaxy-BH correlations quite well (Sijacki et al. 2015). The star formation histories and stellar masses of galaxies show a plausible diversity (Sparre et al. 2015), and the hydrogen reionization history of the Universe can be successfully explained by the high-redshift galaxies forming in Illustris (Bauer et al. 2015). All simulation data has recently been made publicly available (Nelson et al. 2015a), and a comprehensive list of further studies analysing the simulation data can be found online<sup>1</sup>.

While the focus of this work is on the analysis of shocks in the highest-resolution full physics Illustris-1 simulation, we also show results for the lower resolution counterparts Illustris-2 and Illustris-3, and a few selected results for the non-radiative simulations Illustris-NR-2 and Illustris-NR-3. Here the numbers 2 and 3 indicate an 8 and 64 times lower mass resolution compared to Illustris-1, respectively. We note that a more extensive analysis of the non-radiative simulations can be found in the first paper of the series (Schaal & Springel 2015).

## 2.2 Moving-mesh hydrodynamics

The cosmological simulations analysed in this work were run with the AREPO code (Springel 2010), which solves the Euler equations of ideal hydrodynamics on a moving Voronoi mesh by means of a second order finite volume method. This approach improves on traditional hydrodynamic solvers such as smoothed-particle hydrodynamics (SPH) and grid-based schemes by combining advantages of each. In particular, the Euler equations are solved accurately by using a finite volume method on the unstructured Voronoi mesh. The mesh-generating points are moved with the local velocity field, resulting in very small residual mass fluxes across cell interfaces and hence a quasi-Lagrangian and manifestly Galilean-invariant behaviour. This is desirable in the cosmological structure formation problem, because it allows the accurate tracking of highly supersonic flows without large advection errors and additional timestep constraints. Also, the natural adaptivity of the mesh resolution means that the mass per resolution element is automatically kept approximately constant.

Recently, Pakmor et al. (2016) introduced refinements for the moving-mesh scheme in the form of an improved gradient estimator and a suitable Runge-Kutta time integrator. They have shown that with these changes AREPO conserves angular momentum to a high degree and the convergence rate of the code is improved. We note, however, that the Illustris-1 simulation still used an older version of the code.

Moving-mesh simulations are well suited for the analysis of hydrodynamic shocks in cosmology. In a finite volume scheme, the solution is discontinuous across cell interfaces and no artificial viscosity is required, allowing shocks to be captured in principle over one or very few cells. Furthermore, with the moving-mesh approach the resolution at shocks tends to be increased because the

<sup>1</sup> See <http://www.illustris-project.org/results/>

compression of the gas also implies a compression of the grid cells transverse to the shock front, creating an effective enhancement of the resolution particularly in the post-shock region. This feature is very beneficial for constructing an accurate shock finding algorithm, as outlined in the subsequent section.

### 2.3 Shock finding

Constructing an accurate method for identifying hydrodynamic shocks in cosmological simulations proves to be challenging. They are numerically broadened across a few cells and local criteria are therefore not sufficient. Moreover, tangential discontinuities arising in shear flows or contact waves are omnipresent and must not be confused with shocks by the algorithm.

Our method for revealing shocks in moving-mesh simulations is described comprehensively in [Schaal & Springel \(2015\)](#). It is based on a generalization of previous algorithms ([Ryu et al. 2003](#); [Skillman et al. 2008](#); [Hong et al. 2014](#)) to an unstructured mesh and incorporates a number of additional improvements. Here we briefly outline the main steps of the algorithm.

First, we flag cells in regions around shocks, which we call *shock zones* (as in [Skillman et al. 2008](#)). Specifically, a cell is considered part of a shock zone if and only if all of the following three criteria are met. (i) The gas inside the cell is compressed (negative velocity divergence), (ii) the temperature and density gradient must point in the same direction, and (iii) a minimum Mach number jump ( $M \approx 1.3$ ) is exceeded.

In a second step, the shock is reconstructed as a single layer of cells containing the *shock surface*. The corresponding cells are given as those shock zone cells that exhibit the maximum compression along the shock normal, which is defined by means of the temperature gradient. Finally, the Mach number is estimated from the Rankine–Hugoniot temperature jump condition based on the pre- and post-shock temperature values directly outside of the shock zone.

Once the Mach number of the shock is known, its energy dissipation can be calculated, which is the fraction of kinetic energy *irreversibly* converted into thermal energy. The corresponding thermal energy flux  $f_{\text{th}}$  is given by the product of the thermalization efficiency  $\delta(\mathcal{M})$  ([Ryu et al. 2003](#); [Kang et al. 2007](#)) and the inflowing kinetic energy flux,

$$f_{\text{th}} = \delta(\mathcal{M}) \frac{1}{2} \rho_1 (c_1 \mathcal{M})^3, \quad (1)$$

where  $\rho_1$  and  $c_1$  are the pre-shock density and pre-shock sound speed, respectively.

In [Schaal & Springel \(2015\)](#), we have demonstrated that our algorithm can reliably characterize shocks in non-radiative simulations. However, the full physics run Illustris-1 incorporates cooling, star formation and feedback, which poses additional challenges for the shock finding algorithm. It turns out that this necessitates additional algorithmic measures in the detection of shocks in full physics runs, and we hence extend our methodology as follows.

First of all, we need to take care of the star-forming regions. Because the pressure of cells with active star formation is set artificially such that the gas follows an effective equation of state based on a sub-grid multiphase ISM model ([Springel & Hernquist 2003](#)), the sharp transition in the thermodynamic properties between star-forming and non star-forming cells can potentially be interpreted as a shock by our algorithm, distorting our shock statistics. We therefore exclude all cells which lie in density-temperature phase space close to the effective equation of state. Specifically, we ignore de-

tections for which either the pre-shock cell, the post-shock cell, or the cell with the shock fulfils  $\rho > \rho_{\text{sfr}}$  and  $T < 10^5 (\rho/\rho_{\text{sfr}})^{0.2}$  K, where  $\rho_{\text{sfr}}$  is the star formation threshold.<sup>2</sup>

Furthermore, gas cooling and fragmentation due to self-gravity can sometimes result in large gradients of the primitive variables which can appear as correspondingly strong jumps when these gradients are not well-resolved locally. In such a case, the inferred jumps are not consistent with the Rankine–Hugoniot conditions across shocks and should hence not be taken into account. Addressing this issue is primarily important in high density regions. In these locations strong cooling can be present, and moreover, measured energy dissipation rates of spurious detections contribute significantly to the overall dissipation.

We therefore adopt two further precautions in our shock finding algorithm when applied to full physics runs. First, for all tentative shock detections we compare the pre-shock values of pressure, density, and velocity to the corresponding post-shock values, and ignore a detection if one of these variables change in the wrong direction. Recall that the shock direction in our algorithm is determined by means of the temperature gradient.

Secondly, for overdense regions with pre-shock densities  $\delta_b > 1000$ , we calculate in addition to the Mach number based on the temperature jump ( $\mathcal{M}_T$ ), the Mach numbers based on the pressure jump ( $\mathcal{M}_p$ ) and density jump ( $\mathcal{M}_\rho$ ). We then check the mutual consistency of the Mach numbers, and only keep detections with  $f^{-1}\mathcal{M}_p < \mathcal{M}_T < f\mathcal{M}_p$ , and  $f^{-1}\mathcal{M}_\rho < \mathcal{M}_T < f\mathcal{M}_\rho$ . The latter filter is only applied to detections with  $\mathcal{M}_p < 3$  or  $\mathcal{M}_T < 3$ , since the density jump is not sensitive for high Mach numbers. If the different Mach numbers of a cell are consistent, we keep the Mach number inferred by the temperature jump.

With the parameter  $f$  introduced here, the tolerance for accepting detections that deviate from the expected jump conditions can be adjusted. From a theoretical point of view, if a jump in the hydrodynamic variables represents a shock, the Mach numbers inferred by the different jump conditions should be perfectly equal. However, this equality can of course not be expected when measuring shock parameters in numerical simulations due to the unavoidable discretization errors, and consequently,  $f$  should be set to a value well above unity. In this work we adopt  $f = 2$ .

The presence of the unwanted effects described above is demonstrated in Section 5, where we also show that our approach for coping with these limitations is effective. Most importantly, the adopted numerical parameter of  $f = 2$  is a robust choice; varying it within the interval [1.3, 4.0] gives very similar results. This finding indicates that spurious detections of shocks due to poorly resolved local cooling and fragmentation effects indeed strongly violate the Rankine–Hugoniot jump conditions, as otherwise they could not be filtered out so easily.

We want to note that for strongly radiating gas, the jump conditions across shocks deviate from the classic Rankine–Hugoniot conditions derived for non-radiating gas. This is especially the case for regions where the cooling time-scale is very small. In our algorithm the densest regions around star-forming gas are not taken into account, and we hence assume that we can achieve sufficient accuracy by using the unmodified Rankine–Hugoniot jump conditions.

When we analyse the non-radiative run Illustris-NR-2, an important issue arises due to its lack of cosmic reionization. This leads to void regions that are unrealistically cold at low redshift, and hence

<sup>2</sup> The excluded region is indicated by a grey dashed line in the mass-weighted density-temperature histogram discussed in Section 3.2.1.

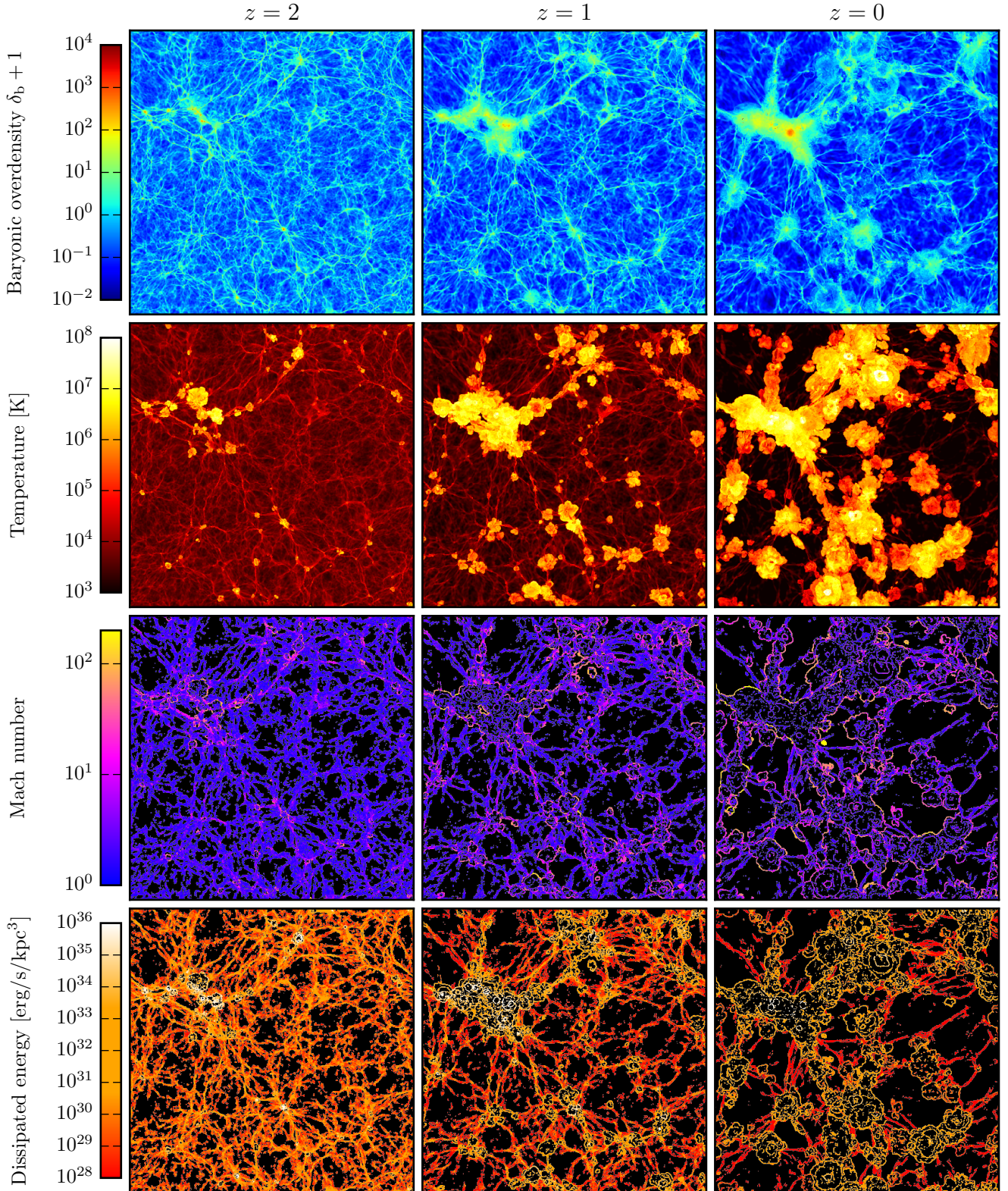


**Figure 1.** Projections of the baryonic overdensity, the temperature, the Mach number field, and the energy dissipation rate density for the full Illustris-1 box ( $75 h^{-1} \text{Mpc}$  per side) at different redshifts. The  $z$ -coordinate of the projections is centred on one of the most massive clusters in the simulation which can be seen in the upper left of each panel ( $M_{200, \text{cr}} = 2.2 \times 10^{14} M_{\odot}$  at  $z = 0$ ). On large scales, accretion shocks on to the cosmic web dominate in the early universe, whereas at late times the radio mode feedback of BHs is omnipresent and creates hot bubbles that shock heat the ambient medium. When cold gas from voids gets shocked, Mach numbers of several hundreds can be reached, but the overall energy dissipated is dominated by the cosmic web. A movie of the shock dynamics in a sub box of Illustris-1 may be accessed online: <https://youtu.be/1CXCrV3i3uw>.

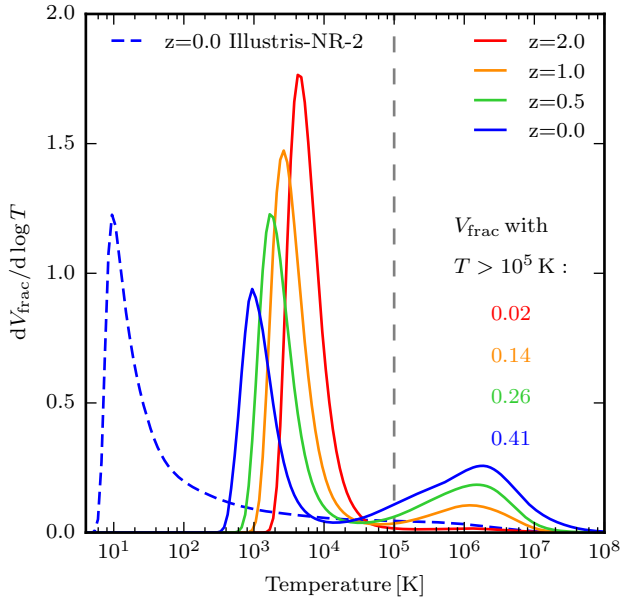


**Figure 2.** Differential volume fraction of the gas in the Illustris-1 simulation as a function of temperature with respect to the whole simulation volume. Due to BH feedback processes the distribution develops a bimodality at late times; at redshift zero a significant volume fraction ( $\approx 40\%$ ) is filled with gas hotter than  $10^5$  K. The positions of the left peaks indicate typical void temperatures in Illustris-1 for the different redshifts. The blue dashed line shows the volume fraction for a non-radiative run as a reference.

the strength of shocks in gas that streams out of voids and accretes on to the cosmic web is overestimated. In order to obtain more realistic Mach numbers for these shocks, we impose a temperature floor of  $10^4$  K on the gas in the post-processing of non-radiative simulations, similar as done in previous studies (Ryu et al. 2003; Skillman et al. 2008; Schaal & Springel 2015). This simple approach is sufficient for our purposes, since the overall energy dissipation at shocks is not very sensitive to the post-processing reionization model. Nevertheless, we note that a more realistic model can be obtained by means of a fitting procedure (Vazza et al. 2009a).

### 3 SHOCK STATISTICS

#### 3.1 Global shock statistics

##### 3.1.1 The global picture

We start by investigating global shock patterns in the Illustris-1 simulation. Fig. 1 presents projections of the mean baryonic overdensity, the mass-weighted temperature, the dissipated energy weighted Mach number, and the mean dissipated energy density at different redshifts. For the density and temperature, the projection depths are 100 kpc, whereas for the quantities inferred from the shock finder we adopt a smaller value of 50 kpc in order to better show the thin shock surfaces. The extent of each panel corresponds to the width of the full simulation volume of  $75 h^{-1}$  Mpc and is centred on one of the most massive objects at  $z = 0$ . The mass inside  $r_{200, \text{cr}}$ , the radius for which the mean overdensity of the halo equals 200 times the critical density of the universe, is  $M_{200, \text{cr}} = 2.2 \times 10^{14} M_{\odot}$  for this central object, similar to the most massive cluster in the volume with  $M_{200, \text{cr}} = 2.3 \times 10^{14} M_{\odot}$ .

At redshift  $z = 2$ , corresponding to a lookback time of around

10 Gyr, the large scale picture is dominated by accretion on to collapsing structures and shocks due to moderate BH feedback. At this time, a typical Mach number for accretion shocks in the cosmic web is  $\mathcal{M} \approx 2$ . The pre-shock gas consists of streams from voids with temperatures around  $4 \times 10^3$  K (see also Fig. 2) and a sound speed of  $c \approx 7 \text{ km s}^{-1}$ , assuming no ionization. A typical velocity in the shock frame for the primordial gas streams is therefore  $v = c\mathcal{M} \approx 15 \text{ km s}^{-1}$ . With time the Mach numbers of shocks around non-linear structures increase. There appear to be two main reasons for this trend. First, the sound speed of voids is lowered by the adiabatic expansion of the universe (although much of this effect is compensated by heating from the UVB) and ever larger infall velocities are produced by the growing masses of objects, and secondly, the BH feedback processes increase in strength with cosmic time.

In particular, between  $z = 2$  and  $z = 1$ , the BH radio mode feedback starts driving hot bubbles that resemble Sedov–Taylor blast waves and feature Mach numbers of several tens in a significant fraction of the simulation volume. These shocks become even stronger at redshift zero when they run into cool and low-density voids, with peak Mach numbers of several hundred. We can estimate the speed of a  $\mathcal{M} = 200$  blast wave by neglecting the speed of the pre-shock gas in the lab frame and assuming a void temperature of  $10^3$  K. This temperature corresponds to a sound speed of  $c \approx 3.4 \text{ km s}^{-1}$  (assuming a mean molecular weight of neutral gas, for simplicity), and we obtain for the velocity of the shock  $v \approx 700 \text{ km s}^{-1}$ . This value is consistent with the velocities inferred by Haider et al. (2016), who compared the diameter of the hot bubbles at different redshifts and reported expansion speeds of  $500 - 1000 \text{ km s}^{-1}$ .

The bottom panels of Fig. 1 show the energy dissipation at shocks, which depends on the Mach number, the pre-shock density, and the pre-shock sound speed. The latter two quantities are high in the interior of non-linear structures and the total energy dissipation at shocks is typically dominated by these locations (Ryu et al. 2003). It can be seen that in the Illustris simulation a high energy dissipation rate is present inside the densest structures between  $z = 2$  and  $z = 1$ , however it seems that at  $z = 0$  the bulk of the thermalization happens in more extended regions. Quantifying these qualitative observations is one of the main goals of this work and will be pursued in subsequent sections.

Large-scale feedback shocks which are omnipresent at  $z = 0$  have the effect of converting BH radio mode feedback energy into thermal energy of the gas. In this way, an extended warm hot intergalactic medium (WHIM) gas phase is created, with temperatures between  $10^5$  K and  $10^7$  K. In Fig. 2, we plot the gas volume fraction per logarithmic temperature bin as a function of temperature for different redshifts. At all times, void regions occupy the largest volume in the simulation, and at  $z = 2$  the distribution peaks around a void temperature of  $5 \times 10^3$  K. With increasing time, this peak shifts towards lower temperatures due to the expansion of the universe and the associated adiabatic gas cooling, reaching  $10^3$  K at  $z = 0$ . Interestingly, the volume distribution develops a bimodality at late times due to a monotonically increasing fraction of gas with temperatures above  $10^5$  K, revealing the extended WHIM created by the BH radio mode feedback. In non-radiative simulations this bimodality is not present, as indicated by the blue dashed line. In Illustris-1, the gas phase with  $T > 10^5$  K occupies around 40% of the volume at  $z = 0$ . Furthermore, it contains more than 60% of the total baryonic mass (Haider et al. 2016).

An important effect of AGN feedback from supermassive BHs is the quenching of star formation in massive systems at late times.

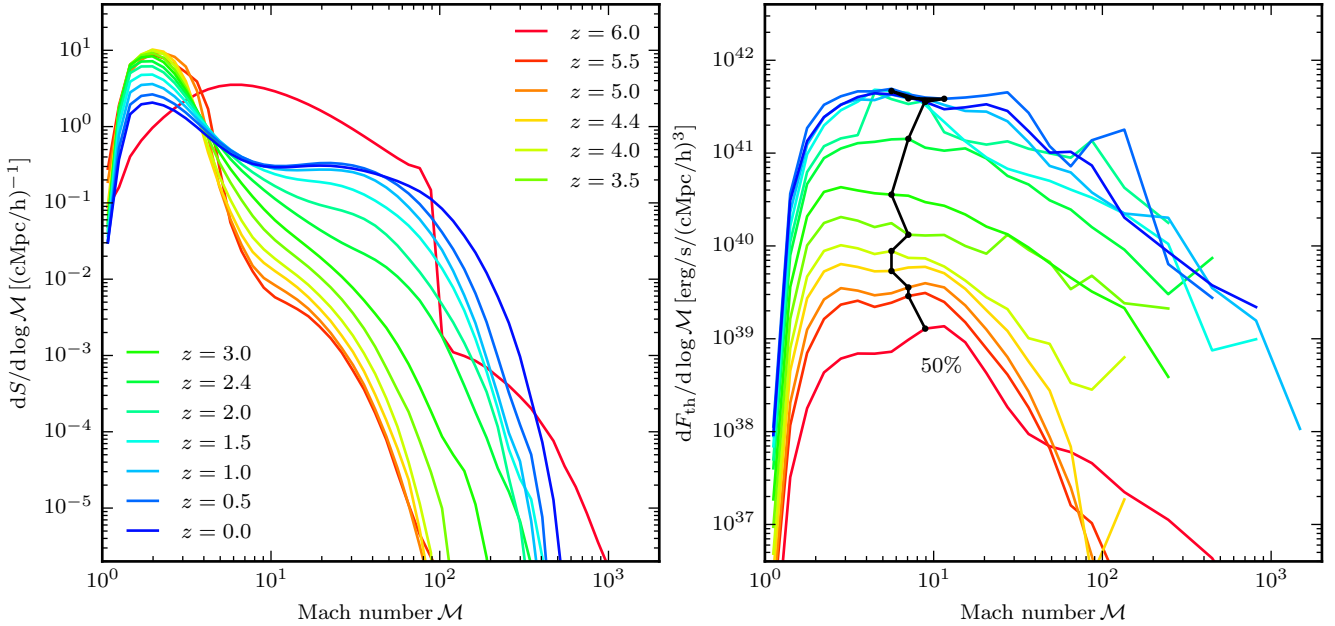


**Figure 3.** *Left-hand panel:* shock surface area per volume as a function of Mach number; this statistic is dominated by external shocks on to the cosmic web. The red line indicates the shock distribution on the eve of reionization, during which voids are heated to  $10^4$  K and the distribution is shifted towards lower Mach numbers. Subsequently, voids merge and cool adiabatically, resulting in a decrease of low Mach number shocks and a larger number of shocks with high Mach numbers. *Right-hand panel:* energy dissipation at shocks as a function of Mach number. At all redshifts, weak and strong shocks contribute similarly to the total thermalization. This is in contrast to the dissipation in non-radiative runs, for which high Mach number shocks are less important. Consequently, the increased dissipation at the high Mach number end can be attributed to shocks created by feedback processes.

In fact, the parameters of the adopted radio mode feedback model have been set in an attempt to match observations of the galaxy stellar mass function (e.g. Bernardi et al. 2013) and the cosmic star formation rate density (e.g. Behroozi et al. 2013). Our results suggest that it would be potentially also very constraining to consider the effects of AGN feedback on the predicted WHIM properties. Unfortunately, this gas phase is difficult to observe due to its low density and comparatively high temperature, resulting in low emission and absorption efficiencies, limiting at present the power of this approach.

Nevertheless, the strong Sedov–Taylor blast wave like shocks due to BH feedback originate in clusters and groups, where the gas density is high. In this environment, as we will showcase in Section 4, these shocks can have higher Mach numbers and larger dissipation rates than cluster merger shocks. The latter can be observed in the local Universe in a few cases directly, and in many others as radio relics. Moreover, shocks associated with AGN have been observed and identified (e.g. Nulsen et al. 2005a,b; Jethava et al. 2008; Blanton et al. 2009; Gitti et al. 2011; Cavagnolo et al. 2011; Randall et al. 2011), however, they are typically of low strength with Mach numbers  $\mathcal{M} \lesssim 2$  and located relatively close to the cluster centre, at distances of at most 200 – 300 kpc. To our knowledge, no strong shocks with properties similar to the AGN feedback shocks in the Illustris simulation have been seen in observations thus far. Their absence hence indicates that the radio mode feedback channel is too strong in the simulation model. This shortcoming of the simulation has also been pointed out by other authors based on other lines of evidence. In particular, as a result of the redistribution of baryons due to the overly strong AGN feedback, the baryon fraction within clusters and groups at  $z = 0$  is underpredicted compared to observations (Genel et al. 2014; Haider et al. 2016).

### 3.1.2 Mach number distributions

In Fig. 3, we show the cumulative shock surface (left-hand side panel) and the energy dissipation at shocks (right-hand side panel) as a function of Mach number for different redshifts. The shock surface is normalized by the simulation volume, and it has therefore units of an inverse length-scale.

For  $z \geq 2$  by far most of the shocks occur between voids and filaments of the cosmic web. The shock surface within haloes is insignificant compared to the total area of shocks, and shocks in the WHIM only contribute non-negligibly for  $z < 2$  (see also Section 3.2.2). Therefore, the shock surface area is dominated by external shocks. The red curve ( $z = 6$ ) indicates the distribution of shocks on the eve of reionization, which in Illustris happens almost instantaneously and is modelled by a uniform time-dependent ionizing background following Faucher-Giguère et al. (2009).

The shock distribution is relatively broad and most of the shocks have Mach numbers around  $\mathcal{M} = 10$ . However, there are also very strong external shocks present with Mach numbers of up to  $\mathcal{M} = 1000$ . These highly supersonic flows are found between the coldest voids and strong filaments or halo outskirts. During the process of reionization the temperature in voids reaches  $\sim 10^4$  K and the distribution is therefore shifted towards lower Mach numbers.

Naively one expects that many weak shocks between voids and the cosmic web disappear during reionization, since the sound speed in the corresponding gas streams exceeds their velocities. However, we do not find that this is the case; the Mach number of a typical external shock merely decreases from  $\mathcal{M} \approx 10$  to  $\mathcal{M} \approx 2$ . We assume that these shock waves can be sustained due to an increase of their pre-shock velocities, which originates from the pressure driven thermal expansion of the filaments during the reionization heating.

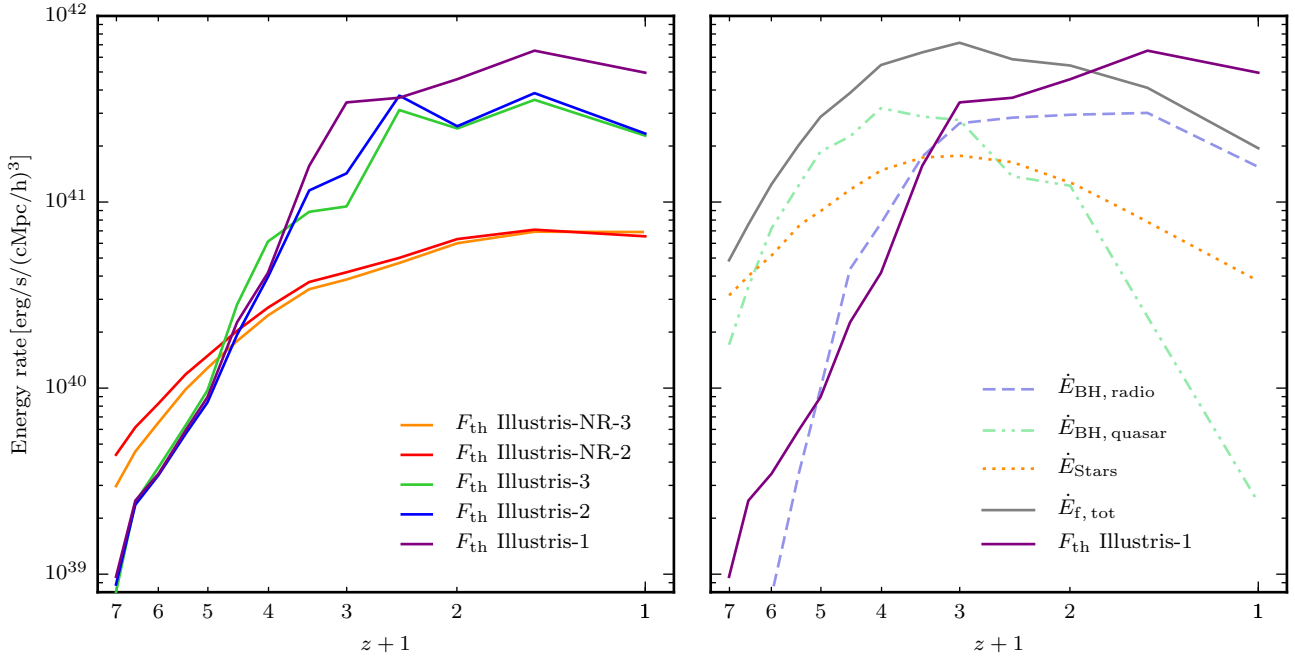


**Figure 4.** *Left-hand panel:* total energy dissipation at shocks as a function of redshift for the different Illustris runs. At late times, the thermalization in the full physics runs is higher by a factor of around 4-8 compared to the non-radiative runs. Moreover, there is good agreement for the runs with resolution levels 2 and 3, whereas the full physics Illustris-1 run shows a stronger dissipation at low redshifts. This effect presumably originates from an increased BH feedback activity in the highest resolution run. *Right-hand panel:* energy dissipation at shocks in the Illustris-1 simulation compared to the energy output of different feedback channels. For redshifts  $z > 1$ , the dissipation stays well below the total energy dumped into feedback processes of stars and BHs, indicating that not all feedback channels produce energetic shocks. On the other hand, there exists a strong correlation at redshifts  $z < 4$  between the energy release by BHs in the radio-mode state and the energy rate dissipated at shocks.

The total shock surface area increases between  $z = 6$  and  $z = 5.5$  (given by the integrals of the curves) by around 7%. Thereafter, it decreases monotonically. We interpret this finding as the creation of a small population of newly created shock waves as the gas responds to the sudden heating during reionization. Note however that this mechanism may be strongly alleviated for a more realistic, gradual reionization history that is stretched out in time, similar to the models arising from radiative transfer methods applied to the Illustris simulation (Bauer et al. 2015).

After reionization ( $z = 5.5$  to  $z = 0$ ), the shock surface of low Mach number shocks progressively decreases, whereas the surface area of high Mach number shocks grows monotonically. This behaviour can be understood if one recalls that the shock surface statistic is dominated by accretion shocks from voids on to the cosmic web. As voids evolve they expand and merge into larger voids (see Fig. 1), which tends to decrease the abundance of low Mach number shocks. At the same time, their gas becomes colder with time (disregarding scenarios such as heating by TeV blazars, see Broderick et al. 2012; Pfrommer et al. 2012), giving rise to a stronger contrast between voids and the cosmic web, and therefore stronger shocks.

Interestingly,  $\mathcal{M} \approx 4.2$  is a peculiar Mach number of the universe; the surface area of shocks with this strength stays roughly constant after reionization. At  $z = 0$ , the total shock surface density reaches a value of  $8.5 \times 10^{-1} \text{ Mpc}^{-1}$  (integral of the blue curve). This number is around 3.4 times higher than what we have found for Illustris-NR-2 (Schaal & Springel 2015). However, in the non-radiative run a large fraction of weak shocks on to the cosmic web is lost by the post-processing reionization modelling in form of a

global temperature floor. We therefore argue that a comparison to Illustris-NR-2 without a temperature floor is more meaningful. In this case we find that in Illustris-1 the total shock surface area is about 1.4 times higher.

The energy dissipation at shocks as a function of Mach number is shown in the right-hand side panel of Fig. 3. This shock property is strongly dependent on the environment and high for regions with high densities ( $f_{\text{th}} \propto \rho_1$ ). Although the shock Mach numbers decrease during the process of reionization, the energy dissipation increases significantly. This can be partly attributed to the triggering of new shocks, but also to the modification of existing ones. We expect that non-linear structures, such as filaments, dynamically respond to the heating by slightly expanding. In this way, the inflowing kinetic energy can be increased.

Throughout cosmic evolution, the shock distribution remains broad and a whole range of Mach numbers contribute comparably. For example, 50% of the thermalization happens at shocks with strengths below  $\mathcal{M} \leq 6 - 10$ , the other half in higher Mach number shocks. As opposed to the low Mach number shocks in the surface statistic, the low Mach number shocks in the energy statistic are shocks well inside non-linear structures, which we refer to as internal shocks. This distribution differs substantially from what is found in non-radiative simulations, where 50% of the dissipation occurs in  $\mathcal{M} < 4$  shocks, and high Mach number shocks are present but do not contribute significantly to the total dissipation.

Non-radiative simulations show a bimodality in the energy statistics, consisting of low Mach number internal shocks which dissipate most of the energy, and high Mach number external shocks processing cold primordial gas (Ryu et al. 2003; Vazza et al. 2011).



Since it can be a source of confusion we want to point out that the bimodality in the energy statistics of non-radiative simulations can not be directly mapped to the surface distribution of shocks. While high Mach number shocks are external shocks, most of the external shocks actually have low Mach numbers (see also Fig. 12 in Vazza et al. 2009a). Moreover, the adopted modelling of reionization can erase weak shocks on to the cosmic web, hence a self-consistent interpretation can ultimately only be achieved if reionization is followed self-consistently during the simulation, as is the case for Illustris-1, albeit with a simplified reionization history.

In the dissipation statistics we measure for the full physics Illustris-1 run, the appearance of energetic high Mach number shocks prevents the development of a bimodality. This difference to the non-radiative simulations is striking, and as we will show later on, the additional shocks can be attributed to feedback processes.

### 3.1.3 Total energy dissipation at shocks

In Fig. 4, we compare the total energy dissipation at shocks across cosmic time for the full physics and non-radiative runs at different numerical resolution. For these simulations the shock finder gives consistent results with respect to resolution. In general, the global dissipation rate shows a shallow but strictly monotonic increase at early times before a saturation sets in. In the full physics runs, a strong increase in the total dissipation rate at shocks can be seen during reionization  $z \approx 6$ , which, as discussed above, presumably originates from the triggering of new shocks and the dynamical response of non-linear structures to the heating. The next four data points between  $z = 5.5$  and  $z = 4$  indicate a power law behaviour, before the energy rate steepens and slightly diverges for the runs with different resolutions. We suggest that the latter feature marks the time when feedback processes from stars and BHs become important for the total energy dissipation at shocks.

From  $z = 4$  to  $z = 2$ , the energy rate rises by more than an order of magnitude and bends sharply thereafter. This sharp bend coincides with the creation of the extended WHIM at  $z = 2$  (recall Fig. 2), indicating that internal shocks are erased in this process. At  $z = 0$ , the simulations Illustris-1, Illustris-2, and Illustris-NR-2 reach final values of  $1.7 \times 10^{41} \text{ erg s}^{-1} \text{ Mpc}^{-3}$ ,  $8.1 \times 10^{40} \text{ erg s}^{-1} \text{ Mpc}^{-3}$ , and  $2.3 \times 10^{40} \text{ erg s}^{-1} \text{ Mpc}^{-3}$ , respectively. In either case, due to the creation of feedback shocks the dissipation in the full physics runs at late times is higher by a factor of several compared to the non-radiative runs.

While the Illustris-3 and Illustris-2 runs give fairly similar results, the dissipation at shocks in the highest resolution run is considerably larger at low redshifts. As we show in Appendix A, the difference originates from high Mach number shocks and correlates with a larger amount of feedback energy released in Illustris-1. Most importantly, between  $z = 2$  and  $z = 0.5$  the BH radio mode feedback is stronger by a factor of around 2. This indicates that BH accretion histories in Illustris are resolution-dependent, and more gas can be funnelled to central regions if the gas dynamics are resolved with a higher resolution.

In order to put the values we measured for the energy dissipation at shocks in Illustris-1 into context, we compare the dissipation rates to other characteristic energy rates in the simulation. Specifically, we want to compare the kinetic energy dissipated at shocks with the energy output of BHs and stars. The energy release by AGN in Illustris-1 scales with the accretion rate  $\dot{M}_{\text{BH}}$  on to the BH and is given by  $\dot{E}_{\text{BH}} = \epsilon \epsilon_r \dot{M}_{\text{BH}} c^2$ . Here,  $\epsilon_r = 0.2$  is the radiative efficiency and  $\epsilon \in \{\epsilon_m, \epsilon_f\}$  the efficiency with which the feedback couples to the surrounding gas. Depending on the accretion rate

the BH is either in the radio feedback mode ( $\epsilon = \epsilon_m = 0.35$ ) or quasar feedback mode ( $\epsilon = \epsilon_f = 0.05$ ). The corresponding criteria are  $\dot{M}_{\text{BH}} < \chi_{\text{radio}} \dot{M}_{\text{Edd}}$  and  $\dot{M}_{\text{BH}} \geq \chi_{\text{radio}} \dot{M}_{\text{Edd}}$ , respectively, where  $\chi_{\text{radio}} = 0.05$  denotes the radio threshold and  $\dot{M}_{\text{Edd}}$  the Eddington accretion rate. Moreover, the injected SNe feedback energy can be inferred by multiplying the cosmic star formation rate density with the SNI energy per stellar mass, which in Illustris-1 has the value of  $\text{egy}_w = 1.09 \times 1.73 \times 10^{-2} \times 10^{51} \text{ erg/M}_{\odot}$  (Vogelsberger et al. 2014a).

In the right-hand panel of Fig. 4, we present the kinetic energy dissipated at shocks in Illustris-1 as well as the energy output of the different feedback channels. The grey lines indicate from top to bottom the BH radio mode energy rate, the BH quasar mode energy rate, the feedback energy rate dumped into stellar winds, and the sum of the feedback energy rates. Several interesting aspects of the adopted galaxy formation model become apparent. First of all, due to the co-evolution of BHs and galaxies, the BH feedback increases at early times in parallel with an increasing SNe energy rate. Later on, the BH accretion rate declines, resulting in a decrease of the BH quasar mode activity and an increase in radio mode activity. The latter trend coincides with an onsetting decline in the star formation rate density, highlighting the importance of the radio mode feedback for quenching star formation in the full physics runs.

For  $z > 0.5$ , the shock energy dissipation stays well below the total feedback energy, indicating that not all feedback channels drive energetic shocks. Especially the AGN quasar-mode feedback and SN feedback offer more net energy than what is detected by shocks for  $z > 3$ . The former heats central regions of galaxies, and presumably much of its energy is radiated away in cooling processes before it can drive energetic shock waves. Galactic winds on the other hand are often launched inside hot haloes where the sound speed is high, making them unlikely to appear as supersonic flows, and in addition, they also suffer from strong radiative cooling losses. Nevertheless, as we will show in Section 4, there are some galaxies which show quasar mode feedback shocks and launch supersonic winds.

For redshifts  $z < 4$ , there is a remarkable correlation between the radio mode AGN feedback rate and the dissipation measured at shocks. We interpret this finding as an indication that this mode is not only able to drive high Mach number and energetic shocks, as seen in Fig. 1, but that these strong feedback blast waves also contribute significantly to the integrated energy statistics at late times.

Hence, it is the BH feedback in the full physics runs which can explain a significant fraction of the overall higher energy dissipation compared to the non-radiative runs. Another source of additional energy dissipation at shocks in the full physics runs could be the presence of gas cooling via radiative processes. In this case, dense streams are formed as well as cold, concentrated gas blobs, which are difficult to disrupt and create ram-pressure shocks absent in the non-radiative simulations.

## 3.2 Environmental dependence of the shock statistics

### 3.2.1 Environmental dependence at redshift zero

In the previous section we have analysed the occurrence of shocks in the Illustris universe and the associated energy dissipation in a global sense as a function of Mach number and redshift. We are now turning to an investigation of the importance of different environments in the thermalization processes during cosmic evolution. For this purpose, we define four disjoint regions based on the gas temperature  $T$  and overdensity  $\delta_b = (\rho_b - \bar{\rho}_b)/\bar{\rho}_b$ , where  $\bar{\rho}_b$  is the

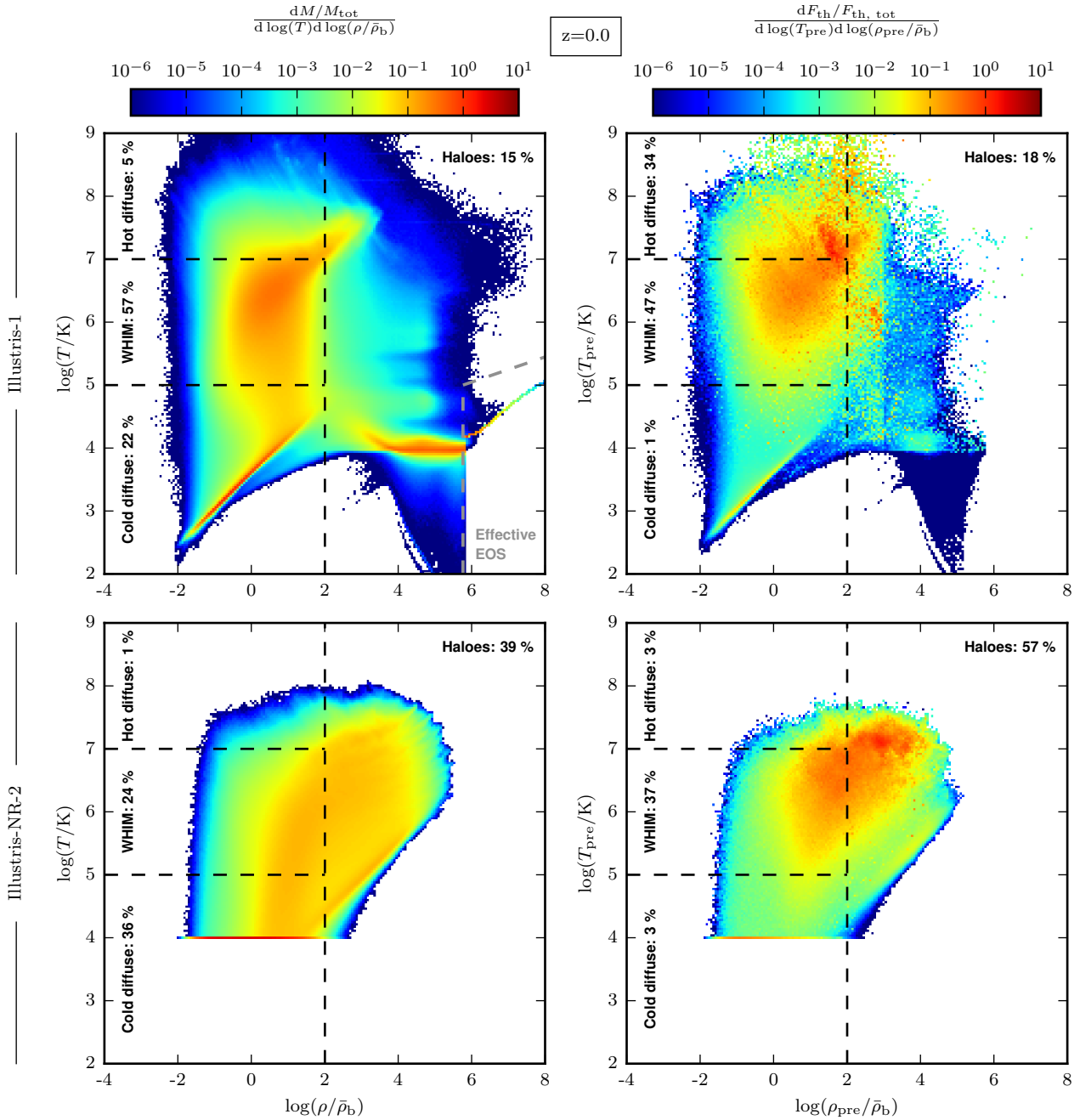


**Figure 5.** Gas density-temperature phase-space diagrams at redshift  $z = 0$  weighted with gas mass (left-hand side panels) and energy dissipation at shocks (right-hand side panels). The latter are constructed with respect to pre-shock gas quantities. The top panels show results for the full physics Illustris-1 simulation, and the bottom panels for the non-radiative Illustris-NR-2 run. In the full physics run, BH feedback processes transfer gas mass from haloes to the ambient medium, creating an extended WHIM region which contains around 60% of the gas mass at  $z = 0$ . Similarly, a large fraction of the energy dissipation is contributed by shocks in the WHIM, which dominate the dynamics of this gas phase. Remarkably, a considerable fraction of dissipation is also present in the hot diffuse phase, where relatively little mass resides.

mean baryon density of the universe. Those environments are cold diffuse gas ( $T < 10^5$  K and  $\delta_b < 100$ ), hot diffuse gas ( $T \geq 10^7$  K and  $\delta_b < 100$ ), the WHIM ( $10^5 \leq T/K < 10^7$  and  $\delta_b < 100$ )<sup>3</sup>, and haloes ( $\delta_b \geq 100$ ).

<sup>3</sup> Some authors define the WHIM environment as  $10^5 \leq T/K < 10^7$ , independent of the gas overdensity. However, in the case of the full physics run our definition is very similar since by far most of the gas in this tem-

perature range is located outside of haloes and therefore has overdensities below 100, as can be seen in Fig. 5.

perature range is located outside of haloes and therefore has overdensities below 100, as can be seen in Fig. 5.

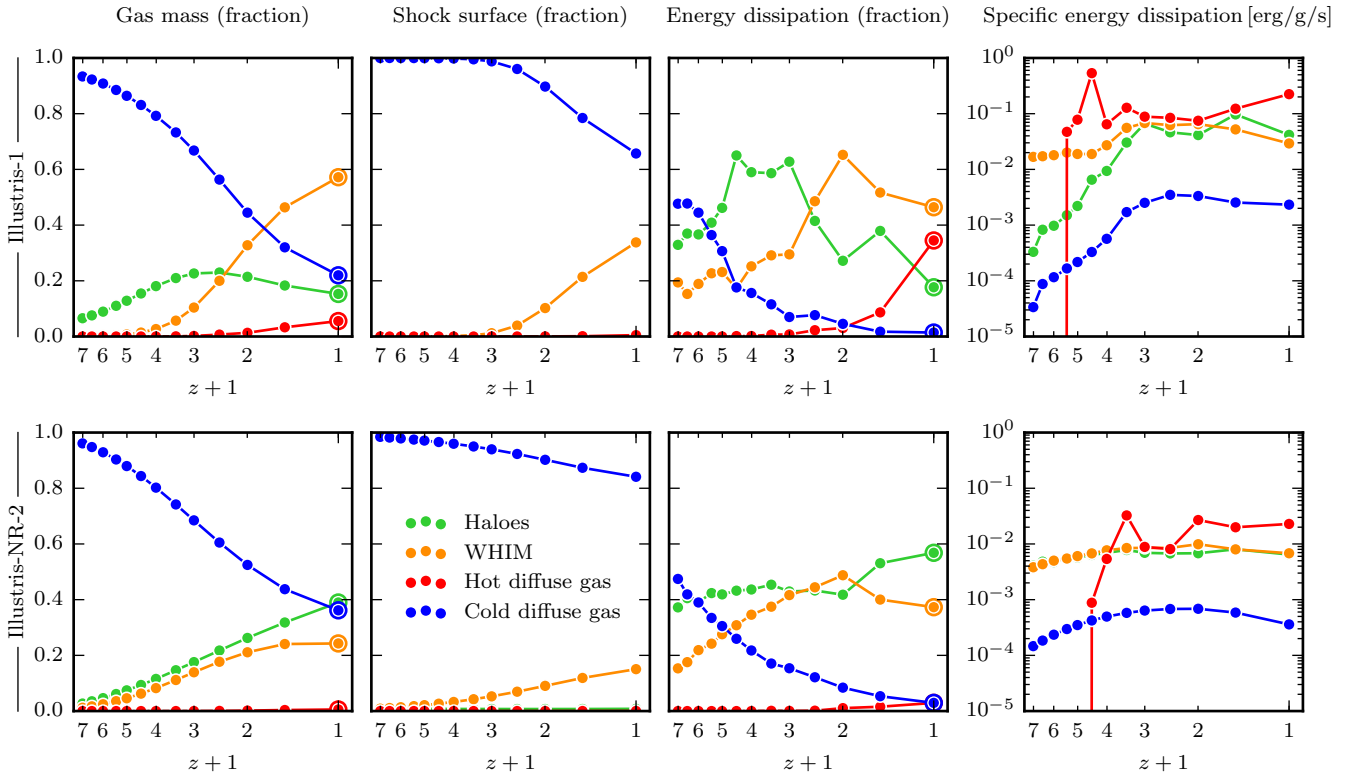


**Figure 6.** Time evolution of the contribution of different environments to, from left to right, the gas mass fraction, the shock surface fraction, the dissipation at shocks, and the dissipation per unit mass. In the full physics as well as in the non-radiative run most of the shock surface area resides in the cold diffuse phase, especially at high redshifts. Between  $z = 3.5$  and  $z = 2$ , shocks inside haloes play the most important role in thermalising energy in Illustris-1, and their relative contribution is significantly higher compared to the non-radiative run. This clearly demonstrates the impact of non-radiative physics, which is most important in this environment. For  $z < 1.5$ , most of the energy is dissipated in the extended WHIM phase and even the hot diffuse phase contributes significantly. The fact that for the latter the shock surface area is very small indicates that this environment is created and heated by individual highly energetic shocks. Interestingly, except for the cold diffuse phase, the different environments have a similar and roughly constant specific energy dissipation for  $z < 3$ .

els on the top and bottom show results obtained for the Illustris-1 and Illustris-NR-2 simulations, respectively. Note that for the non-radiative run, reionization is modelled in post-processing by simply adopting a temperature floor of  $10^4$  K. A large fraction of the mass and dissipated energy of the cold diffuse phase resides in the corresponding individual temperature bin.

Several features in the mass-weighted density-temperature phase diagram of Illustris-1 are apparent (top panel on the left-hand side). In the cold diffuse environment, most of the gas follows a mean equation of state, which is a power law governed by the net effect of photoionization-heating and adiabatic cooling due to the Hubble expansion (Hui & Gnedin 1997). Gas inside the WHIM is characterized by an increased temperature due to shock heating. A correlation can also be seen inside this phase (Davé et al. 2001), which is however less tight and exhibits more scatter. The latter observation is expected due to the variety in number, origin, and properties of shocks governing the dynamics of the WHIM.

Most of the gas above  $\delta_b = 100$  is in a cool phase around  $10^4$  K within galaxies, where photoionization heating and radiative cooling are close to equilibrium (Vogelsberger et al. 2012). Condensed gas above the star formation threshold (vertical grey dashed line) follows an effective equation of state, which represents a subgrid model for a pressurized ISM consisting of a hot and cold phase (Springel & Hernquist 2003). The bulk of gas mass in the Illustris simulation at redshift zero is contained in the WHIM ( $\approx 60\%$ ), fol-

lowed by the cold diffuse phase ( $\approx 20\%$ ), and gas within haloes ( $\approx 15\%$ ).

This gas mass distribution differs significantly from the distribution of the non-radiative Illustris-NR-2 run, in which  $\approx 40\%$  of the gas is contained within haloes, and only  $\approx 25\%$  inside the WHIM at  $z = 0$ . The difference arises mainly due to BH feedback processes in Illustris-1, which transfer gas from haloes to the ambient medium, creating an extended WHIM phase. However, compared to observations the gas mass fractions inside massive haloes ( $M \gtrsim 10^{13} M_\odot$ ) in Illustris-1 at the present epoch appears too low by a factor of several (Genel et al. 2014), indicating that the redistribution is too efficient. For a comprehensive analysis of the mass distribution in the Illustris simulation and comparison to previous work as well as observations, we refer the reader to Haider et al. (2016).

In the non-radiative simulations, for which radiative cooling and feedback is absent, the temperature evolution of the gas is dominated by shock heating on the one hand, and adiabatic cooling due to the Hubble flow on the other hand. Most of the energy dissipation at shocks at  $z = 0$  takes place internally within haloes and filamentary structures, summing up to around 60% of the total dissipation. Those internal shocks typically have high pre-shock sound speeds and therefore low Mach numbers ( $2 \lesssim \mathcal{M} \lesssim 4$ ). However, they dissipate strongly since the inflowing kinetic energy flux is large due to the involved high densities. The second relevant environment is the WHIM, where merger and accretion shocks contribute almost

40% to the total thermalization by shocks. A more extended discussion of shock statistics and morphologies for the Illustris-NR-2 simulation can be found in [Schaal & Springel \(2015\)](#).

We note that for the full physics runs we exclude cells from our shock analysis which are in a region around the effective equation of state, as indicated by the grey dashed lines in the mass-weighted histogram. Moreover, we filter inconsistent jumps above  $\delta_b = 1000$ , and this density threshold can be seen slightly as an edge in the energy dissipation weighted histogram. Its visibility depends on the choice for the parameter  $f$  of our shock finding algorithm, however, as will be shown in Section 5, the choice does not influence the statistics significantly.

In the Illustris-1 simulation, about 80% of the dissipated shock energy is found inside the WHIM and the hot diffuse phase. Compared to the non-radiative run, differences in the WHIM potentially arise from photoionization heating, radiative cooling, and feedback processes from stars and BHs. However, heating due to photoionization increases the gas temperature only to around  $10^4$  K, which is well below the temperature of the WHIM. Moreover, radiative cooling plays only a subdominant role in the evolution of the WHIM ([Davé et al. 2001](#)), since the bulk of the gas has low density.

SN feedback can potentially dump thermal energy into these gas phases, depending on the implementation of this feedback channel and the numerical setup. In Illustris-1, winds are launched in star-forming regions within galaxies and couple to the gas in the near vicinity. These winds can drive shocks and increase the thermal energy of gas within the halo, as shown in Section 4. However, they typically do not reach the virial radius. Consequently, the influence of SN feedback on the WHIM in Illustris-1 can be neglected. We therefore argue that the increased importance of the WHIM and the hot diffuse phase in thermalising kinetic energy originates from BH feedback.

Compared to these phases, the cold diffuse phase is not important in this respect due to its low density. The dissipation within haloes amounts to 15%, which is low compared to the non-radiative run. Note however that in Illustris-1 the overall energy dissipation at late times is higher by a factor of around 8, so compared to the non-radiative simulation the total energy dissipation within haloes is higher.

### 3.2.2 Environmental dependence across cosmic time

In Figure 6, we compare several properties of the different environments across cosmic time. From left to right, we show the gas mass fraction, the shock surface fraction, the energy dissipation rate, as well as the specific dissipation rate. For the shock related quantities the environments are defined with respect to the pre-shock region, and the circled data points at  $z = 0$  correspond to the integrated phase diagrams of Fig. 5. Results for the full physics run are shown in the upper panels, while the lower panels indicate results obtained for the non-radiative run.

As expected, the gas mass fractions in the non-radiative run show a monotonic evolution, in which mass is transferred from low to high density regions. In contrast, BH feedback redistributes baryons in Illustris-1 from haloes to the WHIM and the hot diffuse phase, decreasing the gas mass fraction of haloes at late times to a value below 20%. Moreover, in the full physics run a steeper decrease of the mass in the cold phase is present for  $z < 2$ . This can be explained by the fact that the WHIM does not only grow in mass, but also becomes more spatially extended, as we have seen in Fig. 2.

The shock surface fraction clearly demonstrates that in both kinds of simulations the shock heating of gas in the cold diffuse phase produces the largest contribution to the total shock surface area. Most of these shocks are external shocks, created when pristine gas from voids accretes on to non-linear structures. Only for  $z < 2$  does the WHIM contribute a significant fraction of shock surface area, and furthermore, the cumulative surface area of shocks in haloes and in the hot phase are negligible in comparison.

While measuring the shock surface only reveals the locations of shocks, the energy dissipation quantifies the impact on the thermal history of the gas. Comparing Illustris-1 to Illustris-NR-2 in this respect reveals that between redshifts  $z = 3.5$  and  $z = 2$  a higher fraction of kinetic energy is thermalized within haloes in the full physics run. As can be seen from the left-hand panels, this correlates with a higher halo gas mass fraction in Illustris-1 at early times due to radiative cooling. With more available mass and denser streams more energy can potentially be dissipated. On the other hand, the increase within haloes is abrupt and also coincides with the onset of the BH radio mode feedback at  $z \approx 4 - 3$ . Due to the subsequent mass transfer and expansion of the WHIM, a higher fraction of energy gets dissipated in this environment. Interestingly, shocks in the hot diffuse phase also contribute significantly, although there is only a small increase in the mass fraction and a negligible increase in the shock surface area in this environment. This suggests heating through few but very energetic shocks, pointing once more towards the radio-mode blast waves launched by BHs.

In the panels on the right-hand side we show the specific energy dissipation, which is the dissipation rate per unit mass. Remarkably, apart from the cold diffuse phase, all environments have within a factor of several similar and roughly constant rates for  $z < 3$ . This finding is non-trivial, since although the energy dissipation is proportional to the pre-shock density of the inflowing gas, there is also a strong dependence on the sound speed and the Mach number. The specific dissipation rate in the non-radiative run is around  $10^{-2}$  erg g $^{-1}$  s $^{-1}$ , and for Illustris-1, we measure a 10 times higher value of approximately  $10^{-1}$  erg g $^{-1}$  s $^{-1}$ . In order to put these numbers in context we compare them to the power released in SNe explosions with respect to the mean baryon density of the universe. This rate can be calculated for Illustris-1 as the product of the star formation rate density and the SNII energy per stellar mass,  $P = \text{SFRD} \times e_{\text{gy},w} \approx 0.1 \text{ M}_{\odot}/\text{yr}/\text{cMpc}^3 \times 1.09 \times 1.73 \times 10^{-2} \times 10^{51} \text{ erg}/\text{M}_{\odot}$ , so that we obtain for the specific power a value of  $P_s = P/\bar{\rho}_b = 3.2 \times 10^{38} \text{ erg yr}^{-1} \text{ M}_{\odot}^{-1} = 5.0 \times 10^{-3} \text{ erg g}^{-1} \text{ s}^{-1}$ . Hence, in Illustris-1, the energy rate per unit mass of shocks is higher by a factor of 20 compared to the specific energy rate of stellar feedback.

## 4 SHOCK MORPHOLOGIES ACROSS COSMIC TIME

The aim of this section is to discuss the different shock morphologies found in the Illustris-1 simulation. We mostly present a qualitative overview, with the intention to stimulate a more comprehensive analysis of some of the rich phenomenology exemplified here in future work.

### 4.1 High-redshift accretion shocks

We begin with an investigation of the morphology of accretion shocks. Figure 7 shows the shock environment around some of the biggest haloes in the simulation at  $z = 4$ . As we have seen

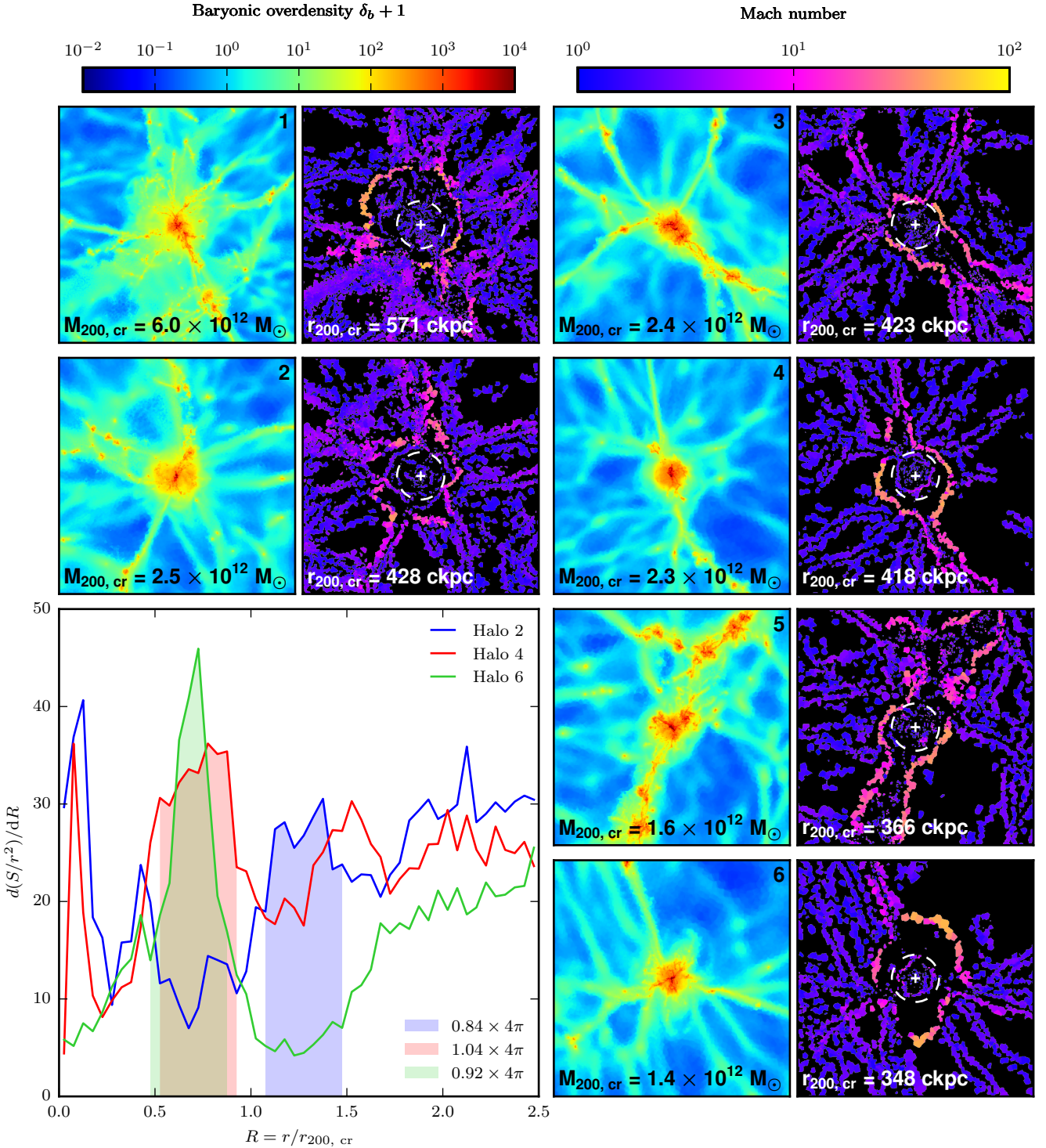


**Figure 7.** Shock environments around some of the largest haloes in the Illustris-1 simulation at  $z = 4$ . Shown are thin projections of the baryonic overdensity and the Mach number, with projection depths of  $0.5 \times r_{200, cr}$  and  $0.1 \times r_{200, cr}$ , respectively. The white circles correspond to the virial radii, and their values are given in comoving kiloparsec at the bottom of the Mach number panels. In all haloes strong accretion shocks can be seen, which are typically located outside of the virial radius. Moreover, these outer accretion shocks can get penetrated by filaments, depending on their size and hydrodynamic properties. Interestingly, in several cases a second inner accretion shock is formed, especially when the flow inside the penetrating filament is smooth (haloes 2, 4, and 6). The lower-left panel shows the shock surface distribution as a function of radius for the corresponding haloes. In all three cases, the inner accretion shock covers a solid angle of approximately  $4\pi$ , indicating that they are spherical.

in Section 3.1, the violent BH radio mode feedback, which operates during low accretion rates, is still largely absent at this time. Moreover, we do not expect many shocks from the quasar mode feedback, and the stellar feedback operates on smaller scales compared to the one under consideration. We have checked the environment of the same haloes in the non-radiative Illustris-NR-2 run (not shown), and find shocks with very similar Mach numbers and locations. Consequently, the shocks seen in Fig. 7 are indeed accretion shocks.

The importance and character of shocks in the formation of gaseous haloes as well as their role in galaxy formation have been a lasting topic in the literature. In the classical two-stage galaxy formation theory (White & Rees 1978) infalling gas gets shock-heated to the virial temperature before it can cool and settle into a disc, forming stars inside out. The pressurized atmosphere of the gaseous halo can either be created due to thermalization in a strong accretion shock, or through a succession of smaller shocks inside the halo. The scenario in which the gas gets shock heated to the virial temperature before it cools and fragments into stars is termed the ‘hot/slow’ mode of gas accretion. If the cooling time is much shorter than the dynamical time, which is the case for low-mass galaxies, gas can also be accreted in a ‘cold/rapid’ mode without being shocked (Fardal et al. 2001; Birnboim & Dekel 2003), something that is also present in the original theory of hierarchical galaxy formation (White & Frenk 1991). Furthermore, there may exist a third mode, in which an outer accretion shock gets penetrated by cold filaments, feeding the central galaxy with cold and unshocked gas (e.g. Dekel & Birnboim 2006; van de Voort & Schaye 2012).

The haloes shown in Fig. 7 have masses well above  $M_{200, \text{cr}} > 10^{12} M_{\odot}$  and are among the most massive haloes at  $z = 4$ . The specific haloes have been selected for illustrating the wide variety of occurring shock features. For haloes in this mass range, theoretical models predict the existence of stable accretion shocks (Dekel & Birnboim 2006). The distance of the outer accretion shock from the halo centre as inferred from non-radiative simulations is on average around  $1.3 \times r_{200, \text{cr}}$  (Schaal & Springel 2015). However, the accretion shock can sometimes also be found significantly further outside ( $\lesssim 2 \times r_{200, \text{cr}}$ ), especially if the halo is in a non-equilibrium state after a major merger event (Nelson et al. 2016).

For all haloes in Fig. 7, the presence of an outer accretion shock is evident, with varying Mach number depending on the environment. The accretion shock is stronger if gas is infalling directly from voids, as it is the case for halo 4 in the bottom-right, and halo 6 in the top-right direction, with Mach numbers up to  $\mathcal{M} = 100$ . The corresponding accretion flows are highly supersonic due to their low sound speed. On the other hand, if the halo is surrounded by weak filaments whose gas is shock heated at the outer accretion shock, the typical Mach numbers are significantly lower (e.g. halo 2,  $\mathcal{M} \approx 10$ ). In several locations, we see that strong filaments are able to penetrate the outer accretion shock. This preferentially happens for filaments with high gas densities and velocities, resulting in a large ram pressure  $p_{\text{r}} \propto \rho v^2$ .

Interestingly, although the masses of the haloes are similar, we find a considerable variety among their interior shock morphologies. Halo 1 dissipates thermal energy internally by a network of complex weak shocks. This network is likely induced by recent merger events, since it also coincides with an increased outer accretion shock pointing towards a non-equilibrium system. Strikingly, in haloes 2, 4, and 6, a second accretion shock located inside of the outer accretion shock can be seen. These shocks can potentially be

formed if there is cold gas from filaments crossing the outer accretion shock unshocked.

The lower left panel of Fig. 7 shows the radial shock surface distribution of these haloes, and for each halo the inner accretion shock can clearly be seen as a peak in the distribution. Moreover, by integrating the peaks one obtains the solid angles covered by shocks at the corresponding radii. We integrate each curve at the location of the inner accretion shock over an interval of size  $0.45 R$ , which accounts for the deviation from perfect sphericity of the shocks. The integrals of the inner accretion shocks of haloes 2, 4, and 6 amount to  $0.84 \times 4\pi$ ,  $1.04 \times 4\pi$ , and  $0.92 \times 4\pi$ , respectively, indicating that they are largely spherical.

Haloes 3 and 5 are also penetrated by strong filaments, but in these cases no inner spherical accretion shocks can be found. On the other hand, these haloes experience a more clumpy accretion flow compared to halo 4 and 6, which might prevent the formation of the inner spherical shock.

The existence of inner and outer accretion shocks is consistent with recent work by Nelson et al. (2016), who analysed gas accretion on to  $10^{12} M_{\odot}$  haloes at  $z = 2$  by means of cosmological hydrodynamic zoom simulations<sup>4</sup>. In addition to a strong virial shock at around  $1.3 \times r_{200, \text{cr}}$ , they report for their analysed haloes that inflows which are not shocked at the virialization boundary are significantly heated inside the virial radius. This happens at a distinct distance from the centre, typically at  $\lesssim 0.5 \times r_{200, \text{cr}}$ , and only thereafter the gas cools and accretes on to the central galaxy in the examined systems.

Fig. 8 shows a zoom on to halo 4 that focuses on projections of the Mach number and temperature field. Additionally, in the left-hand panel the direction and magnitude of the peculiar gas velocity is visualized by the orientations and colours of arrows, respectively. The halo has a virial mass of  $M_{200, \text{cr}} = 2.3 \times 10^{12} M_{\odot}$  and is surrounded by a strong outer accretion shock with Mach numbers of  $\mathcal{M} = 40 - 50$ . Such shock strengths are expected for relatively cool accretion flows from voids and weak filaments. Moreover, gas inside the highlighted filament is dense and fast enough to penetrate this outer shock and thermalize further in, where the halo pressure is higher. The accretion flow from the filament gets accelerated towards the potential minimum and reaches a velocity of around  $500 \text{ km s}^{-1}$  relative to the halo center. With a pre-shock temperature of  $10^5 \text{ K}$  and assuming full ionization, this configuration corresponds roughly to a Mach number 10 shock, consistent with the value obtained by the shock finder. Moreover, given the location inside the virial radius, this shock can be considered very strong.

Interestingly, while the filament crosses the outer shock in the vertical direction, there are also inner accretion shocks in perpendicular directions, forming as a whole an approximately spherical inner accretion shock. This phenomenon can be understood by investigating the temperature map of the halo, which is shown in the right-hand panel of Fig. 8. The grey contour line at  $T = 3 \times 10^4 \text{ K}$  corresponds roughly to the pre-shock temperature of the outer accretion shock, and the black contour line at  $T = 1.5 \times 10^6 \text{ K}$  highlights the inner temperature structure of the halo. It can be seen that the cold stream from the filament does not only create a bow shock, it also flows around it and mixes with gas shock-heated at the outer accretion shock. In this way, the temperature and sound speed of the latter is decreased such that it gets shocked a second time in order to reach the virial temperature. The black contour line

<sup>4</sup> Although this study also uses the AREPO code, very different simulation physics have been used compared to the Illustris runs.

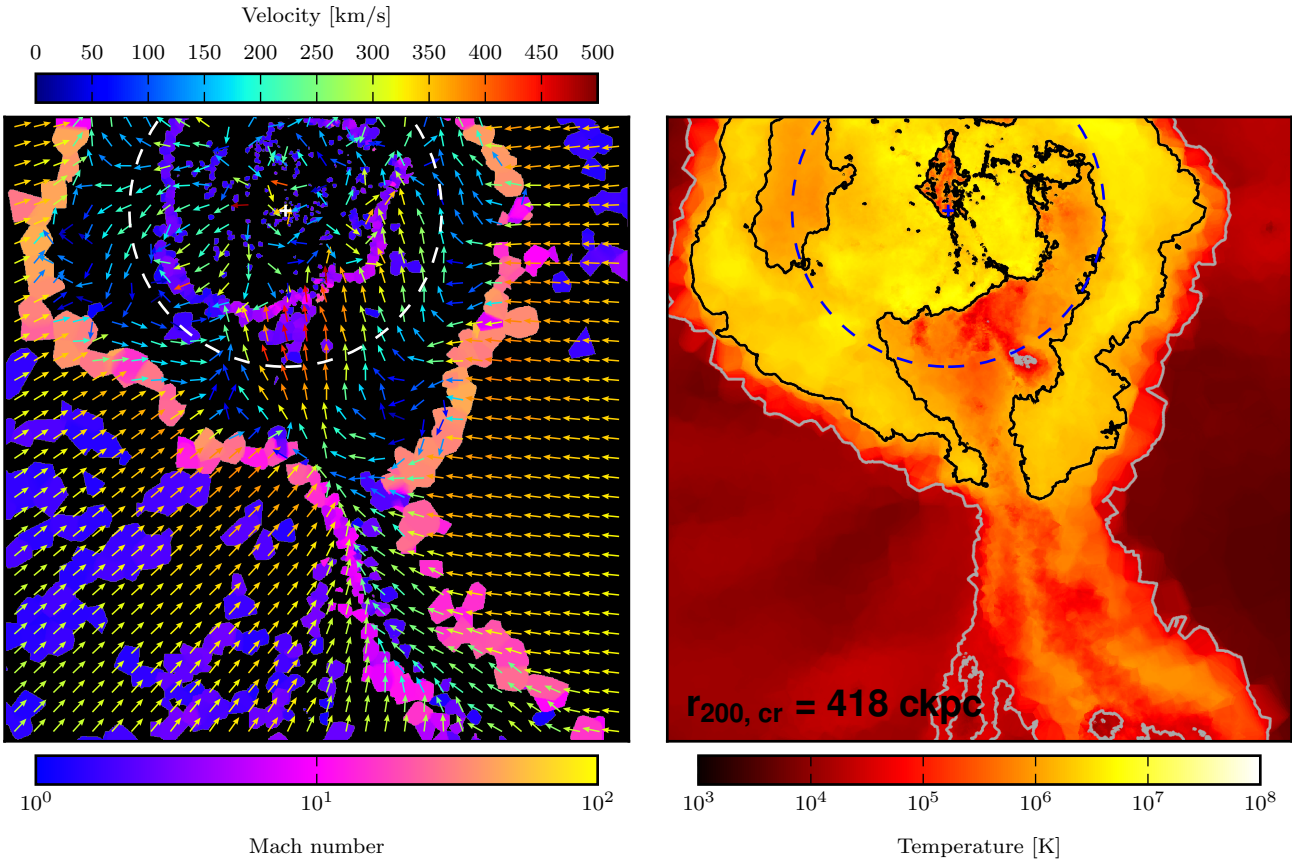


**Figure 8.** Zoom on to a halo with a double accretion shock (halo 4 from Fig. 7). The left-hand panel shows a thin projection of the Mach number field, as well as the direction and magnitude of the peculiar gas velocity field (coloured arrows). On the right-hand side panel, the mass-weighted mean temperature is projected, together with 2D contours at  $T = 3 \times 10^4$  K (grey) and  $T = 1.5 \times 10^6$  K (black) for visual guidance. The dashed circles correspond to the virial radius,  $r_{200, \text{cr}} = 418$  ckpc. A vertical filament penetrates the outer accretion shock and channels cold gas into the interior. The cold stream coming from the bottom is accelerated and heated at a smaller radius by a strong shock ( $M \approx 10$ ). Moreover, since the cold phase mixes with gas shock heated at the outer accretion shock, a roughly spherical inner accretion shock is formed.

also indicates that the left part of the inner accretion shock forms mainly due to a cooling stream from the top; as can be seen in Fig. 7 there is a counterpart of the highlighted filament.

This discussion raises the question whether the interpreted shock surfaces change with simulation resolution, and to which degree they are modified by radiative physics. We show in Appendix A the halo of Fig. 8 for different resolutions and find that a very similar inner accretion shock is obtained in the Illustris-2 run. Moreover, it is also present in the non-radiative simulation Illustris-NR-2, although in this case the inner shock is less spherical and the shape is dominated by the two bow shocks in the directions of the filaments.

It would be instructive to infer the abundance of the double accretion shocks, ideally in an automated way. However, this proves to be difficult, since a very similar signature in the differential shock surface distribution is created by ellipsoidal accretion shocks, which peak at the radial positions of the semi-principal axes (see Schaal & Springel 2015, Fig. 6, Halo 8). Moreover, the gas resolution in smaller mass haloes is too low at  $z = 4$  in Illustris-1 for this kind of analysis. Nevertheless, it would be interesting in future simulations to shed light on the questions if, when, and to which extent gas inside virialized structures of different masses got shock-heated. This could be accomplished in zoom simulations by running the shock finder on the fly and recording a shock history for every gas parcel, a natural extension of a temperature history

based analysis by means of Monte Carlo tracer particles (Genel et al. 2013; Nelson et al. 2013).

## 4.2 Galaxy and galaxy cluster shocks

In Fig. 9, we show the shock environment around some of the biggest haloes in the simulation at  $z = 2$ . We have chosen these specific haloes in order to showcase the different occurring shock morphologies, and they are therefore not necessarily representative for a typical system. The cluster at the top accretes streams of substructures which induce a complex network of low Mach number shocks in the cluster interior. Due to the high central densities they are very effective in thermalising kinetic energy, as can be seen in the top panel on the right-hand side. Moreover, these merger shocks in combination with the accretion shocks at the outskirts are thought to be one of the main drivers of intracluster turbulence (e.g. Dolag et al. 2005; Vazza et al. 2009b; Miniati 2014, 2015).

Merging clusters often emit unpolarized diffuse synchrotron emission over large scales, observed as giant radio haloes (Ferrari et al. 2008; Feretti et al. 2012). These observations indicate the presence of magnetic fields and relativistic electrons. The latter can acquire their energy via reacceleration due to magnetohydrodynamic turbulence, or have a hadronic origin through creation in the decay chain of accelerated protons colliding with thermal protons

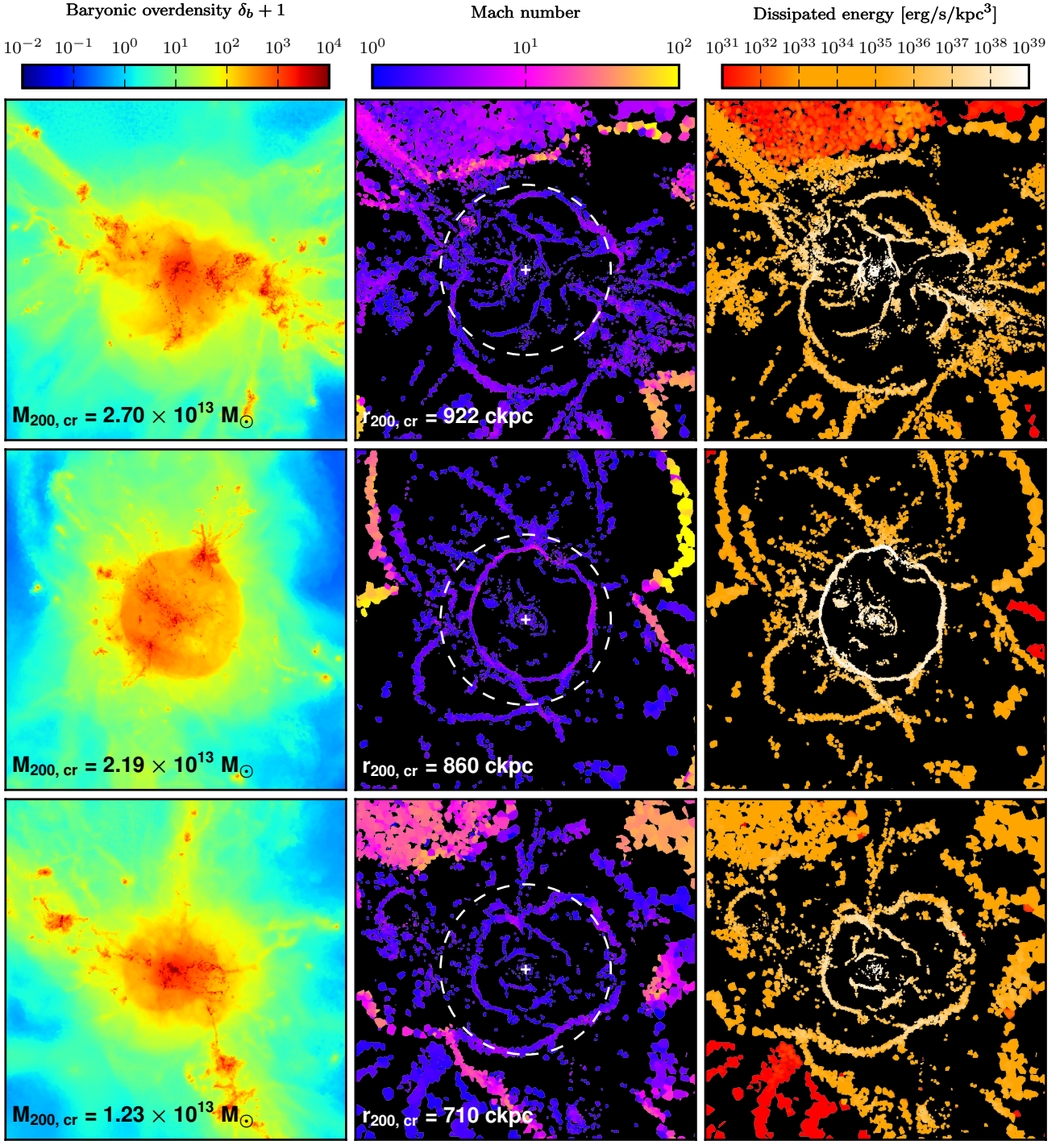


**Figure 9.** Zoom on to some of the most massive galaxy clusters at  $z = 2$  in Illustris-1. Shown are projections of the baryonic overdensity, the Mach number, and the energy dissipation, with depths of  $0.5 \times r_{200, \text{cr}}$  for the density, and  $0.1 \times r_{200, \text{cr}}$  for the shock related quantities. In the halo of the first row, merger activities can be seen which induce a complex network of internal shocks. These shocks as well as the stimulated supersonic turbulence inside the cluster are potential cosmic ray particle accelerators. The BH of the halo displayed in the middle row recently released a large amount of thermal energy, resulting in an energetic Sedov–Taylor like blast wave feedback shock. The halo at the bottom presumably underwent a major merger recently, as revealed by the arc-shaped merger remnants opposite to each other. Interestingly, we detect strong shocks on to cosmic sheets around the haloes at the top and at the bottom.



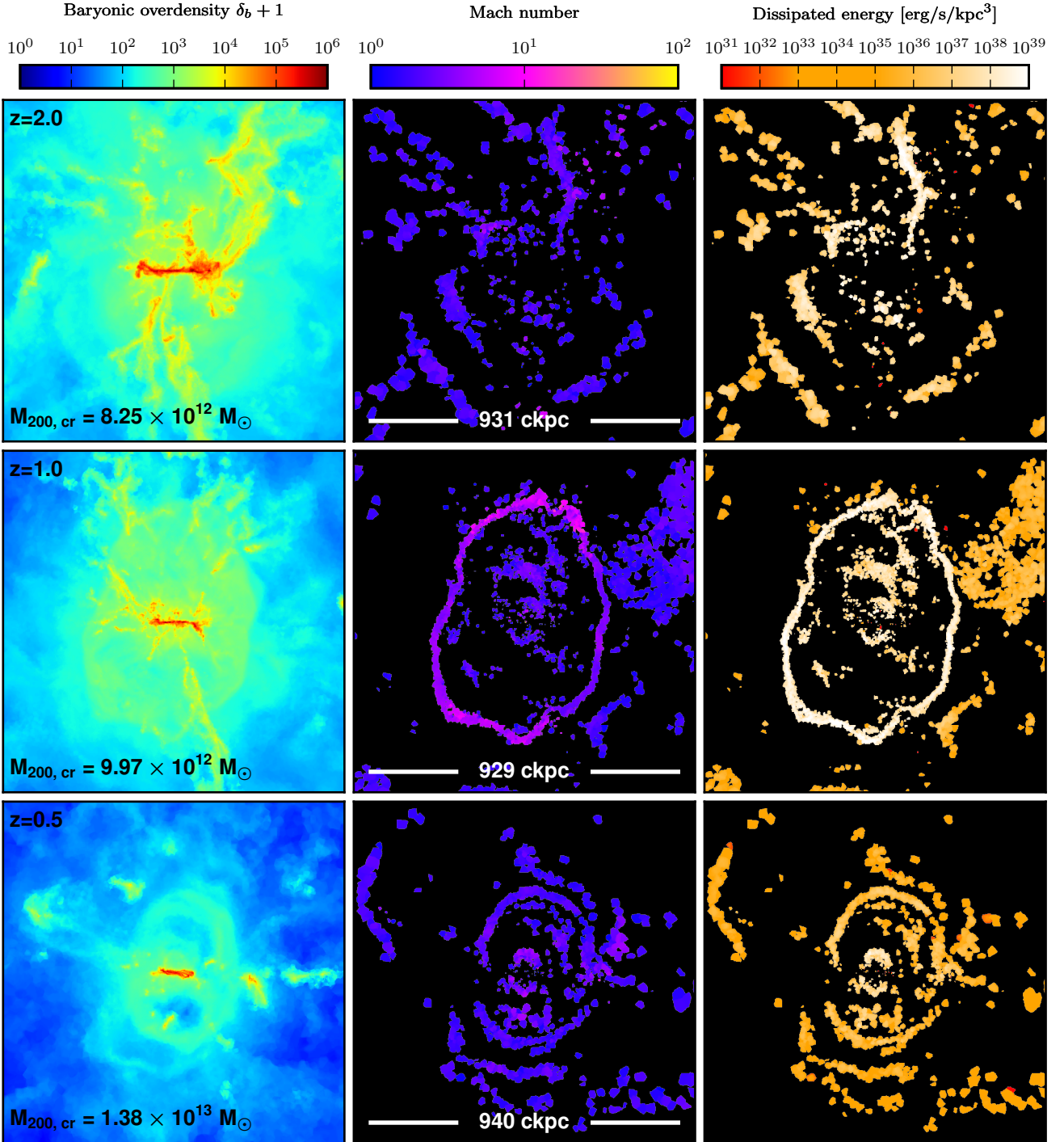


**Figure 10.** Zoom on to disc galaxies at three different redshifts. The projections show a square with a size of  $1.5 \times r_{200, cr}$  per side and have a depth of  $0.08 \times r_{200, cr}$ . Different morphologies can be seen with, from top to bottom, complex inflow and outflow patterns, recent BH activity, and supersonic stellar winds. Also on these scales the most energetic shocks are provided by AGN.

(Enßlin et al. 2011; for a recent review see Brunetti & Jones 2014, and references therein). On the other hand, directly accelerating electrons from the thermal pool via second-order Fermi acceleration proves to be difficult from a theoretical point of view, since the required acceleration time is long. Recent limits on the  $\gamma$ -ray emission of clusters suggest a cosmic ray pressure of around 1%–2% of

the cluster thermal pressure, depending on the assumptions (Arlen et al. 2012; Ackermann et al. 2014; Ahnen et al. 2016).

The galaxy cluster in the middle panel recently launched an AGN feedback shock, in the form of a thermal pressure dominated Sedov–Taylor like blast wave. The Mach numbers across the shock surface are fairly high, considering also the fact that it has not yet escaped the hot halo atmosphere. Moreover, this shock is highly

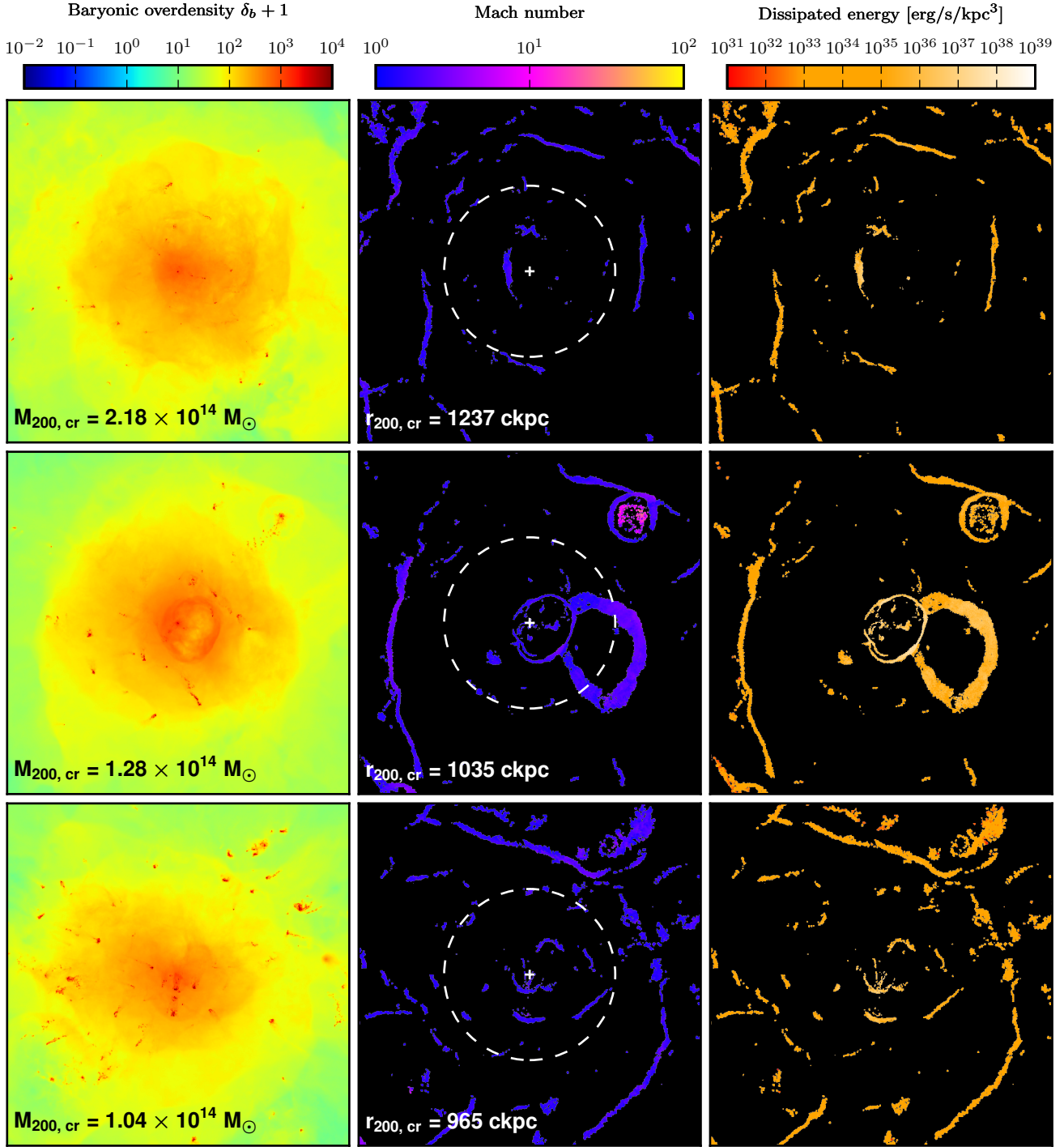


**Figure 11.** Projections of some of the most massive haloes at  $z = 0$ , with depths of  $0.5 \times r_{200, \text{cr}}$  and  $0.1 \times r_{200, \text{cr}}$  for the overdensity and the shock-related quantities, respectively. Due to BH feedback the gas of these haloes has been substantially diluted, and most of the present shocks are remnants of this process. However, as can be seen in the middle panels, new BH feedback shocks are still created at the present epoch. In the halo at the bottom the accretion of numerous substructures can be seen, giving rise to bow-shaped shocks.

energetic at its current location. We have measured the total energy dissipation inside the box  $[4 \times r_{200, \text{cr}}]^3$  and find that it is around two times higher compared to the dissipation rate in the cluster at the top, and around nine times higher than the dissipation of the cluster shown at the bottom of the figure. For BHs remaining predominantly in the radio mode, these kinds of feedback shocks

are launched relatively frequently. We hence infer that these blast waves make an important contribution to the high value of the energy dissipation rate in haloes between  $z = 3.5$  and  $z = 2$ .

The bottom panels show a galaxy cluster with corrugated shock surfaces. The surfaces are typically located where the ram pressure of the inflow matches the thermal pressure of the cluster. In this

way, for homogeneous inflows, the shock locations trace equipotential lines of the cluster. In the displayed halo, three major filamentary streams are present, and the accretion shock shows a concavity in their direction. Interestingly, the filaments at the upper left span a cosmic sheet, and we detect high Mach number accretion shocks at this location. A similar morphology can be seen for the halo in the top panels. Consequently, the large area of Zeldovich pancakes can provide a very interesting site for particle acceleration near clusters. In the central region of the galaxy cluster, merger remnants with positions opposite to each other are visible; we assume that this halo underwent a major merger event very recently.

In the local Universe, synchrotron radiation originating from merger remnants can be observed in the form of radio relics. Considering the strength and dissipation rate of the AGN feedback shock, we argue that this shock should also be observable. Up to now, most of the radio haloes and relics are observed at redshifts  $z \lesssim 0.5$  (Feretti et al. 2012), however, this may largely be due to present sensitivity limits. But as we show in more detail below, in Illustris AGN feedback shocks are also created for lower redshifts, up to the present epoch. Since the shocks appear strong enough to create strong synchrotron emission, the lack of clear observational detections of such signals indicates that the radio mode feedback is likely too strong in Illustris-1. This argument shows that shock properties could be used in the future to constrain or validate the modelling and parameter space of feedback models used in state-of-the-art cosmological simulations. In particular the modelling of radio and gamma-ray emission represents a promising link between simulations and observations (Pfrommer et al. 2008; Pinzke & Pfrommer 2010; Vazza et al. 2013; Pinzke et al. 2015; Hong et al. 2015).

The Illustris simulation contains around 40000 well-resolved galaxies with an encouragingly realistic mix of morphologies and kinematic properties (Vogelsberger et al. 2014b,c; Genel et al. 2014; Snyder et al. 2015). In Fig. 10, we show zoomed in view of three late-type systems with masses of around  $10^{13} M_{\odot}$  at, from top to bottom, redshifts  $z = 2$ ,  $z = 1$ , and  $z = 0.5$ , in order to investigate shock signatures around such systems. The displayed images have a length of  $1.5 \times r_{200, \text{cr}}$  on a side, i.e. the virial radius corresponds roughly to the distance between the corners and the centres of the images.

The spiral galaxy at  $z = 2$  interacts with the circumgalactic medium (CGM) via a complex pattern of inflows and outflows, resulting in several shocks inside the hot halo. However, this example demonstrates the limitation of our shock finder in combination with Illustris. Poorly resolved gradients in the outskirts of the galaxy result in patches of shocks, rather than in well-defined shock surfaces. Moreover, since we filtered out detections of shocks near star-forming regions that are governed by the subgrid model, it is not possible to see shocks within the galaxy, for example around spiral arms.

Recent BH activity is apparent for the galaxy at  $z = 1$ . Given the shock morphology we suspect that in this case the feedback originates from the quasar mode. The shape of the shock is less spherical compared to the blast waves created by the radio-mode feedback, and moreover, it has apparently been launched very centrally. This is unlikely to happen in the case of the radio mode feedback, for which a random injection within a sphere around the BH is adopted. Nevertheless, the energy dissipation at this shock is exceedingly high, indicating that also on galactic scales BH feedback drives the most energetic shocks. This is especially expected when the BH reaches the end stages of a phase of exponential growth

(during which it shines as a quasar) and shuts down its own growth through energy feedback (Di Matteo et al. 2005).

Interestingly, the galaxy at  $z = 0.5$  launches supersonic galactic winds, and we are able to detect the associated shocks. These winds are dominated by kinetic energy and become particularly effective when they are strongly collimated in disc-dominated systems. The role of SN driven winds in the Illustris galaxy formation model (Vogelsberger et al. 2013) is to slow down star formation, suppress cosmological gas inflow (Nelson et al. 2015b), and enrich the CGM with metals (Bird et al. 2014; Marinacci et al. 2014; Suresh et al. 2015b,a). As the Mach number and energy dissipation fields reveal, the heating through the winds can be effectively mediated by shocks. We note that the morphology of galactic wind shocks can be clearly distinguished from other feedback shocks through the typical consecutive arcs they produce well inside the virial radius.

Finally, in Fig. 11, we show projections of three of the most massive systems in Illustris-1 at  $z = 0$ . These cluster-sized haloes underwent violent BH feedback processes for much of their cosmic evolution, such that their gas is heavily diluted at  $z = 0$ . This also manifests itself in an ambient WHIM gas phase that is spatially very extended. The shock morphologies in these environments are dominated by a small number of very fine surfaces, indicating that these systems are less dynamic and more relaxed compared to the massive haloes at higher redshifts. As can be seen in Fig. 4, the energy release rate of BHs decreases substantially for  $z < 0.5$ , but the shocks found around the second halo demonstrate that new strong feedback shock waves are still created at these times.

## 5 METHODOLOGY VARIATIONS

Our shock-finding algorithm can potentially report spurious detections of shocks due to large but poorly resolved gradients in regimes which are dominated by gravitational forces, or where the equations of ideal hydrodynamics are modified by an imposed equation of state. This can for example be the case if gas enters gravitational free fall after rapid cooling, or for gas around the effective equation of state used to model the star-forming medium. The associated jumps in the hydrodynamic variables should not be confused with shocks. We have therefore introduced in Section 2.3 the filtering parameter  $f$ , which controls the amount of tolerance we allow for inconsistencies between the jumps inferred from different hydrodynamic quantities. In this section, we briefly test the dependence of our results on this nuisance parameter of our shock detection scheme.

In Fig. 12, we compare the shock environment around one of the biggest haloes at  $z = 2$  when no shock filtering is applied (right-most panel) to the case when active filtering with our standard settings is applied (middle panel). Without the filter, there is a spray of loosely connected shocked cells with high Mach numbers whose locations coincide with the highly overdense gas of star-forming regions. A large fraction of these shocks is likely spurious and arises because our shock detection algorithm is misled by the transition to a non-ideal gas equation of state at the star formation threshold.

If the filter is active, cells which are potentially part of the pressurized ISM, or may have been recently, are excluded from the shock finding procedure. Moreover, we require for all detections that the jump directions of the hydrodynamic quantities are consistent with the temperature gradient, and for potential shocks having pre-shock densities  $\delta_b > 1000$  we explicitly verify different Rankine–Hugoniot jump conditions. As outlined in Section 2.3, only those detections are kept which have consistent Mach num-

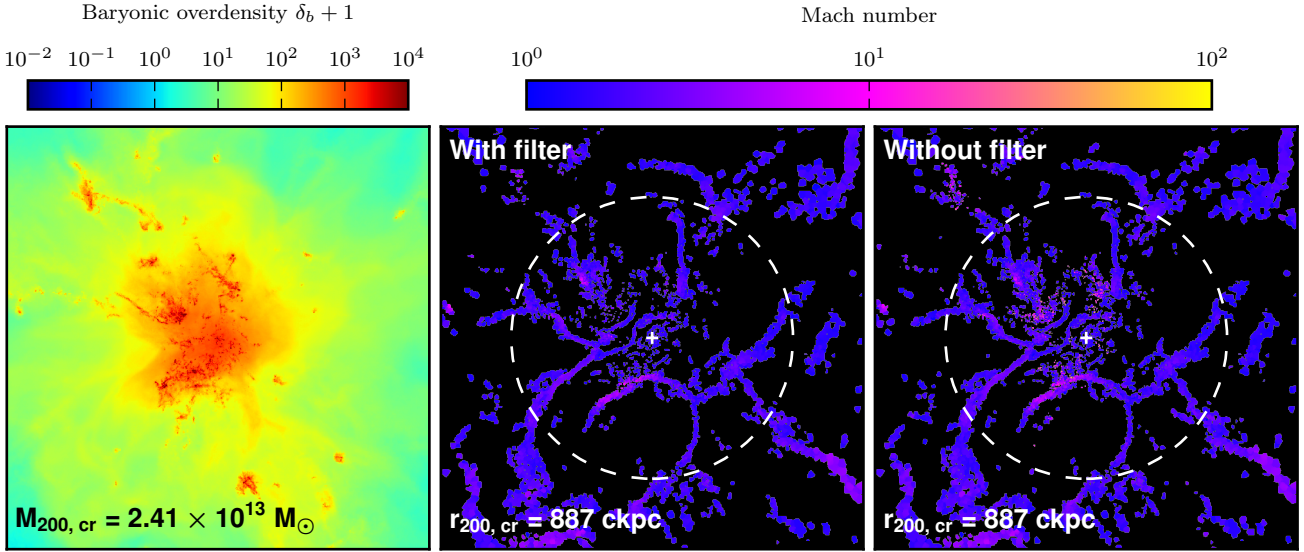


**Figure 12.** Demonstration of the impact of filtering against spurious shock detections due to non-hydrodynamic physics. The middle panel shows the shock environment around a halo at  $z = 2$  obtained with our improved shock finding methodology. In the right-hand side panel the result without filtering star-forming gas and inconsistent jumps can be seen. The difference seems to be very subtle, however, the spurious detections dominate the total energy dissipation over a wide range of redshifts, as shown in Fig. 13. It can therefore be very important to further improve shock finder implementations developed for non-radiative simulations before applying them to full physics runs.

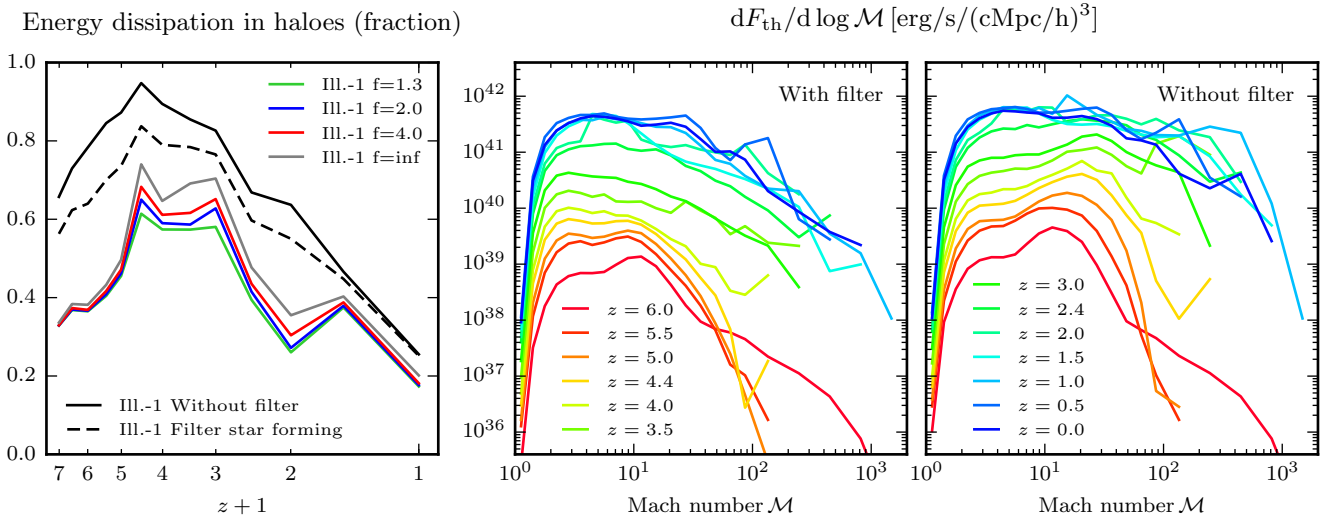


**Figure 13.** *Left-hand panel:* contribution of shocks in haloes ( $\delta_b \geq 100$ ) to the total dissipation rate for different tolerance values  $f$ , as well as for the case when no filter, or only the filter for the star-forming region is used. The result does not change significantly for  $f \in [1.3, 4]$ , and hence our choice of  $f = 2$  is very robust. This furthermore indicates that unwanted spurious detections are highly inconsistent with the full set of Rankine–Hugoniot jump conditions. *Middle and right-hand panels:* energy dissipation at shocks as a function of Mach number with and without the improved shock finding methodology, respectively. Especially at high redshifts, the spurious detections enhance the measured energy dissipation by a factor of several.

bers within a tolerance  $f$ , inferred by the temperature, pressure, and density jump conditions. For this work we adopt the value  $f = 2$ , which, as can be seen in the middle panel, filters most of the unwanted detections. Spurious detections are mainly present in high overdensity regions, and we find that at  $z = 0$  around 12% of all potential shocks are filtered by our algorithm due to inconsistent jump directions or Mach numbers.

While in the Mach number projections the spurious detections are only visible as a subtle feature, they can nevertheless significantly

change the shock energy statistics due to their high pre-shock densities. In Fig. 13, we compare the energy dissipation at shocks as a function of Mach number with and without the filter. In the middle panel, we give the results for our standard filter configuration as a reference; this plot is the same as in Fig. 3. The right-hand side panel shows results obtained if no filter is used. Especially for high redshifts and Mach numbers  $\mathcal{M} > 10$ , the measured energy dissipation is greatly enhanced in this case. The total dissipation (integral

of the curve) without applied filter is higher by factors of 2.9, 8.5, and 1.4 at redshifts  $z = 6$ ,  $z = 3.5$ , and  $z = 0$ , respectively.

In the left-hand panel of Fig. 13, we investigate the robustness of our filter with respect to the introduced parameter  $f$ . Shown is the contribution of haloes to the total dissipation rate for different filter configurations. The black curve is obtained if no filter is used at all. For the black dashed curve, we filter gas around star-forming regions, but we do not perform consistency checks. The grey curve shows the result obtained if the star-forming region is filtered and in addition the consistency of the jump directions with the temperature gradient is demanded. Finally, the coloured curves indicate results with the full filter being active, but for different tolerance values  $f$ . Even though the parameter range  $f \in [1.3, 4]$  is rather large, there are only changes at the 10% level in the results. This means that the spurious detections are strongly violating the consistency relations of the Rankine–Hugoniot jump conditions, allowing them to be reliably filtered with our approach and a parameter value of  $f = 2$ . Also note that it is not sufficient to only remove detections around star-forming regions. The consistency condition is also required to obtain fully reliable results.

An important lesson from our investigation is that shock finders designed and tested with non-radiative simulation are unlikely to work reliably for full physics runs unless they are refined further. Applying them blindly risks that systematic biases in measures like the energy dissipation statistics are introduced. The severity of these biases will depend on the radiative and feedback physics realized in the simulation code, as well as on the particular shock finding technique that is used. For example, while Kang et al. (2007) and Hong et al. (2014) find only minor effects in runs including cooling and star formation, the energy dissipation tail at high Mach numbers reported in Pfrommer et al. (2007) might partially originate from spurious shocks around the adopted subgrid star formation model.

## 6 DISCUSSION AND SUMMARY

Cosmological hydrodynamical simulations are now able to successfully describe the co-evolution of dark matter and baryons in remarkable detail. As the modelling of the involved physical processes is refined, it is important to explore novel ways of accessing the information content provided by such simulations. Thus far, the analysis of properties of the diffuse gas has often been restricted to considerations of the most basic quantities, such as (spherically averaged) density and temperature values. However, gas dynamics has much more to offer. In this study, we have for the first time analysed the shock statistics in a state-of-the-art high-resolution simulation of galaxy formation, the Illustris project.

We have characterized the shocks in the Illustris universe by post-processing the simulations with AREPO’s shock finding algorithm (Schaal & Springel 2015). AREPO accurately solves the Euler equations of ideal hydrodynamics with a finite volume method on a moving-mesh and is able to capture shocks precisely. In combination with our shock finder we can reliably detect and characterize the hydrodynamic shocks and associated quantities.

From a theoretical point of view, shocks are of fundamental interest. They arise from the non-linearity of the hydrodynamic equations and are therefore a manifestation of one of the key characteristics of the governing equations. In order to understand the gas dynamics in a complex system, much can be learned by merely investigating the locations and strengths of shocks. Moreover, shock quantities provide a reduced dataset of the gas in hydrodynamic

cosmological simulations, which can be used to simplify the analysis of large output files<sup>5</sup>.

In this work we have focused on analysing shocks in the full physics Illustris-1 simulation. In order to put the results for the most important statistics into context, we also compared with results obtained for the non-radiative run Illustris-NR-2. The differences in shock statistics and shock morphologies between the two kinds of simulations arise due to physics beyond ideal gas dynamics in Illustris-1. Most importantly, this simulation accounts for cosmic reionization, radiative cooling and heating of gas, star formation and BH growth, as well as their associated feedback processes. In what follows, we summarize our most important findings.

- **Improvement of the shock finding methodology.** In the full physics runs, we have discovered spurious shock detections in star-forming regions and at the edges of cold, poorly resolved self-gravitating clumps. They originate from modifications of the gas state by the subgrid ISM model and cooling physics, respectively. We have shown that these spurious detections severely change the energy dissipation statistics if the problem is just ignored. We have thus introduced improvements to our shock finding routines that were not part of the method we developed originally for non-radiative runs. First of all, we excise star-forming regions in our shock finding algorithm. Secondly, we ignore detections for which the hydrodynamic jumps are inconsistent with the shock direction given by the temperature gradient, and last but not least, we demand that shocks in overdense regions consistently fulfil the Rankine–Hugoniot jump conditions for several different hydrodynamic quantities. We have demonstrated that these conservative filters are necessary to reliably find and characterize hydrodynamic shocks in the Illustris simulation. We anticipate similar problems for other shock finders developed for non-radiative runs, and hence caution against applying them in unmodified form to full physics runs.

- **Impact of reionization.** We find in Illustris-1 a significant increase in the measured shock surface area as well as in the total energy dissipation between redshifts  $z = 6$  and  $z = 5.5$ . This coincides with reionization, which is modelled by a uniform UV background following Faucher-Giguère et al. (2009) and happens in the simulation almost instantaneously at  $z \lesssim 6$ . We interpret this finding as the signature of a temporary population of weak shocks associated with the dynamical response of the gas to the sudden heating during reionization, which for example lets gas stream off the shallow potential wells of very low-mass dark matter haloes. Quantitatively, this result certainly depends on the details of the reionization transition.

- **Shock surface area.** Until  $z \approx 1$  by far the largest shock surface area can be found between voids and the cosmic web. The cumulative shock surface statistic is therefore dominated by the number and temperature of voids. During structure formation, small voids merge to form larger ones, and the number of low Mach number shocks decreases. At the same time, voids are coupled to the Hubble flow and cool adiabatically, resulting in an increase in the occurrence of high Mach number shocks. Moreover, we find that the number of shocks with  $\mathcal{M} \approx 4$  stays roughly constant with time. For  $z < 1$  a significant number of shocks can also be found in the WHIM, with a maximum contribution of around 34% at  $z = 0$ . After reionization, the total shock surface area decreases monotonically, nevertheless, at the present epoch we find a total shock sur-

<sup>5</sup> In the case of Illustris-1, a snapshot consists of around  $1.2 \times 10^{10}$  resolution elements and has a size of about 2.5 terabytes.

face area in Illustris-1 which is around 1.4 times larger compared to the corresponding non-radiative run.

- **Energy dissipation.** By measuring the energy dissipation rate at shocks the impact on the thermal history of the gas can be inferred. In non-radiative runs, the overall energy dissipation grows with cosmic time, and when its Mach number dependence is considered a bimodality in the energy statistics can be seen; internal low Mach number shocks dissipate most of the energy, whereas external shocks have high Mach numbers but are much less energetic (Ryu et al. 2003). Remarkably, we find for Illustris-1 that shocks with Mach numbers smaller and larger than  $\mathcal{M} \approx 10$  contribute about equally to the overall dissipation, and no bimodality is observed. For this full physics simulation, we attribute the large population of high Mach number shocks to feedback processes.

Between  $z = 3.5$  and  $z = 2$ , most of the energy dissipation occurs within haloes, where cooling processes create structures with large density contrasts. It is also around this time that the radio mode feedback of BHs first kicks in, which is associated with the low accretion rate state of the BHs. We show that this type of feedback drives energetic high Mach number shocks and creates an extended WHIM gas phase. We measure a total energy dissipation in Illustris-1 which is higher by a factor of around 8 for  $z < 2$  compared to the corresponding non-radiative run. It is plausible that a large fraction of this additional dissipation originates from the BH radio mode feedback.

As a result of the redistribution of baryons at low redshifts to the WHIM, this phase gains importance as a site for energetic shocks. At  $z = 0$  around 80% of the dissipation occurs at shocks in the WHIM and in the hot diffuse phase ( $T > 10^7$  and  $\delta_b < 100$ ). This is in strong contrast to the corresponding non-radiative simulation, in which about 60% of the thermalization happens inside haloes at the present epoch. At  $z = 0$  the total dissipation rate in shocks in Illustris-1 amounts to  $1.7 \times 10^{41} \text{ erg s}^{-1} \text{ Mpc}^{-3}$ . Moreover, except for the cold diffuse gas phase, all environments have similar and approximately constant specific dissipation rates for  $z < 3$ . This value is approximately  $10^{-1} \text{ erg g}^{-1} \text{ s}^{-1}$ .

- **Shock morphologies.** We have investigated accretion shocks of haloes with mass above  $10^{12} M_{\odot}$  at  $z = 4$  when feedback processes influencing large scales are still largely absent. As expected for haloes in this mass range, we find accretion shocks which are typically located outside of the virial radius. However, we see filaments which can penetrate the accretion shock, and their gas streams enter the halo unshocked. Interestingly, we discover that the formation of a spherical accretion shock further inside the halo is still possible in this case. Our finding of an accretion mode involving both an inner and an outer accretion shock is consistent with recent work by Nelson et al. (2016), who analysed the thermal gas structure of  $10^{12} M_{\odot}$  haloes at  $z = 2$  in zoom simulations.

We have showcased different shock morphologies of galaxies and galaxy clusters at  $z \leq 2$ . Those include complex networks of weak shocks in cluster interiors, merger remnants, strong BH feedback shocks, shocks on to cosmic sheets, as well as supersonic stellar winds and complex flows around galaxies. By visually comparing the properties of an AGN feedback shock with a merger remnant shock, we argue that the radio mode feedback is too strong in Illustris-1. This conclusion is consistent with the findings of Genel et al. (2014) and Haider et al. (2016), who report a baryon fraction inside clusters which is too small at the present epoch and also attribute this finding to the radio mode feedback channel. This also shows that the properties of shocks can be used in future state-of-the-art cosmological simulations for constraining the modelling and parameter space of feedback implementations.

These results underline the importance of feedback processes for shock statistics, and the large impact they have on the shocks that are present. As we expect the strongest shocks to be efficient accelerators that produce non-thermal particle distributions, shock statistics combined with upper limits on cosmic ray densities could be developed into a powerful constraint for viable feedback models. Future simulation models will also try to take the cosmic ray particle populations self-consistently into account. In this case further refinements of the shock detection methodology are needed in order to cope with mixtures of ordinary gas and cosmic rays (Pfrommer et al. 2016).

## ACKNOWLEDGEMENTS

It is a pleasure to thank Andreas Bauer, Rainer Weinberger, Christian Arnold, Christine Simpson, Robert Grand, Martin Sparre, Federico Marinacci, Rahul Kannan, Lorenzo Sironi, and Blakesley Burkhart for useful comments and insightful discussions. Moreover, the authors would like to thank the referee for a constructive report which helped improving this paper. KS and VS acknowledge support through subproject EXAMAG of the Priority Programme 1648 SPPEXA of the German Science Foundation, and the European Research Council through ERC-StG grant EXAGAL-308037. CP acknowledges support through the ERC-CoG grant CRAGSMAN-646955. SG acknowledges support provided by NASA through Hubble Fellowship grant HST-HF2-51341.001-A awarded by the STScI, which is operated by the Association of Universities for Research in Astronomy, Inc., for NASA, under contract NAS5-26555. DS acknowledges support by the STFC and the ERC Starting Grant 638707 “Black holes and their host galaxies: co-evolution across cosmic time”. LH acknowledges support from NASA grant NNX12AC67G and NSF grant AST-1312095. KS, VS, RP, and CP like to thank the Klaus Tschira Foundation, and KS acknowledges support by the IMPRS for Astronomy and Cosmic Physics at the University of Heidelberg.

## REFERENCES

- Ackermann M., et al., 2014, *ApJ*, **787**, 18  
 Ahnen M. L., et al., 2016, *A&A*, **589**, A33  
 Akamatsu H., Kawahara H., 2013, *PASJ*, **65**  
 Arlen T., et al., 2012, *ApJ*, **757**, 123  
 Axford W. I., Leer E., Skadron G., 1977, International Cosmic Ray Conference, **11**, 132  
 Battaglia N., Pfrommer C., Sievers J. L., Bond J. R., Enßlin T. A., 2009, *MNRAS*, **393**, 1073  
 Bauer A., Springel V., Vogelsberger M., Genel S., Torrey P., Sijacki D., Nelson D., Hernquist L., 2015, *MNRAS*, **453**, 3593  
 Behroozi P. S., Wechsler R. H., Conroy C., 2013, *ApJ*, **770**, 57  
 Bell A. R., 1978a, *MNRAS*, **182**, 147  
 Bell A. R., 1978b, *MNRAS*, **182**, 443  
 Bernardi M., Meert A., Sheth R. K., Vikram V., Huertas-Company M., Mei S., Shankar F., 2013, *MNRAS*, **436**, 697  
 Bird S., Vogelsberger M., Haehnelt M., Sijacki D., Genel S., Torrey P., Springel V., Hernquist L., 2014, *MNRAS*, **445**, 2313  
 Birnboim Y., Dekel A., 2003, *MNRAS*, **345**, 349  
 Blandford R. D., Ostriker J. P., 1978, *ApJ*, **221**, L29  
 Blanton E. L., Randall S. W., Douglass E. M., Sarazin C. L., Clarke T. E., McNamara B. R., 2009, *ApJ*, **697**, L95  
 Bondi H., 1952, *MNRAS*, **112**, 195  
 Bondi H., Hoyle F., 1944, *MNRAS*, **104**, 273  
 Bourdin H., Mazzotta P., Markevitch M., Giacintucci S., Brunetti G., 2013, *ApJ*, **764**, 82  
 Broderick A. E., Chang P., Pfrommer C., 2012, *ApJ*, **752**, 22

- Brüggen M., van Weeren R. J., Röttgering H. J. A., 2011, *Mem. Soc. Astron. Italiana*, **82**, 627
- Brüggen M., Bykov A., Ryu D., Röttgering H., 2012, *Space Sci. Rev.*, **166**, 187
- Brunetti G., Jones T. W., 2014, *International Journal of Modern Physics D*, **23**, 1430007
- Cavagnolo K. W., McNamara B. R., Wise M. W., Nulsen P. E. J., Brüggen M., Gitti M., Rafferty D. A., 2011, *ApJ*, **732**, 71
- Chabrier G., 2003, *PASP*, **115**, 763
- Dasadia S., et al., 2016, *ApJ*, **820**, L20
- Davé R., et al., 2001, *ApJ*, **552**, 473
- Dekel A., Birnboim Y., 2006, *MNRAS*, **368**, 2
- Di Matteo T., Springel V., Hernquist L., 2005, *Nature*, **433**, 604
- Dolag K., Vazza F., Brunetti G., Tormen G., 2005, *MNRAS*, **364**, 753
- Enßlin T. A., Biermann P. L., Klein U., Kohle S., 1998, *A&A*, **332**, 395
- Enßlin T., Pfrommer C., Miniati F., Subramanian K., 2011, *A&A*, **527**, A99
- Erlar J., Basu K., Trasatti M., Klein U., Bertoldi F., 2015, *MNRAS*, **447**, 2497
- Fardal M. A., Katz N., Gardner J. P., Hernquist L., Weinberg D. H., Davé R., 2001, *ApJ*, **562**, 605
- Faucher-Giguère C.-A., Lidz A., Zaldarriaga M., Hernquist L., 2009, *ApJ*, **703**, 1416
- Feretti L., 2005, in Sjouwerman L. O., Dyer K. K., eds, *X-Ray and Radio Connections*. (arXiv:astro-ph/0406090)
- Feretti L., Giovannini G., Govoni F., Murgia M., 2012, *A&ARv*, **20**, 54
- Ferrari C., Govoni F., Schindler S., Bykov A. M., Rephaeli Y., 2008, *Space Sci. Rev.*, **134**, 93
- Finoguenov A., Sarazin C. L., Nakazawa K., Wik D. R., Clarke T. E., 2010, *ApJ*, **715**, 1143
- Genel S., Vogelsberger M., Nelson D., Sijacki D., Springel V., Hernquist L., 2013, *MNRAS*, **435**, 1426
- Genel S., et al., 2014, *MNRAS*, **445**, 175
- Gitti M., Nulsen P. E. J., David L. P., McNamara B. R., Wise M. W., 2011, *ApJ*, **732**, 13
- Haider M., Steinhauser D., Vogelsberger M., Genel S., Springel V., Torrey P., Hernquist L., 2016, *MNRAS*, **457**, 3024
- Hinshaw G., Larson D., Komatsu E., Spergel D. N., Bennett C. L., Dunkley J., Nolte M. R., Halpern 2013, *ApJS*, **208**, 19
- Hong S. E., Ryu D., Kang H., Cen R., 2014, *ApJ*, **785**, 133
- Hong S. E., Kang H., Ryu D., 2015, *ApJ*, **812**, 49
- Hoyle F., Lyttleton R. A., 1939, *Proceedings of the Cambridge Philosophical Society*, **35**, 405
- Hui L., Gnedin N. Y., 1997, *MNRAS*, **292**, 27
- Jethava N. N., Hardcastle M. J., Ponman T. J., Sakelliou I., 2008, *MNRAS*, **391**, 1052
- Kang H., Ryu D., Cen R., Ostriker J. P., 2007, *ApJ*, **669**, 729
- Katz N., Weinberg D. H., Hernquist L., 1996, *ApJS*, **105**, 19
- Kennel C. F., Edmiston J. P., Hada T., 1985, *Washington DC American Geophysical Union Geophysical Monograph Series*, **34**, 1
- Keshet U., Waxman E., Loeb A., 2004, *New Astron. Rev.*, **48**, 1119
- Krymskii G. F., 1977, *Akademiia Nauk SSSR Doklady*, **234**, 1306
- Macario G., Markevitch M., Giacintucci S., Brunetti G., Venturi T., Murray S. S., 2011, *ApJ*, **728**, 82
- Malkov M. A., O’C Drury L., 2001, *Rep. Progress Phys.*, **64**, 429
- Marinacci F., Pakmor R., Springel V., Simpson C. M., 2014, *MNRAS*, **442**, 3745
- Markevitch M., 2010, preprint, (arXiv:1010.3660)
- Markevitch M., Gonzalez A. H., David L., Vikhlinin A., Murray S., Forman W., Jones C., Tucker W., 2002, *ApJ*, **567**, L27
- Markevitch M., Govoni F., Brunetti G., Jerius D., 2005, *ApJ*, **627**, 733
- Miniati F., 2014, *ApJ*, **782**, 21
- Miniati F., 2015, *ApJ*, **800**, 60
- Miniati F., Ryu D., Kang H., Jones T. W., Cen R., Ostriker J. P., 2000, *ApJ*, **542**, 608
- Miniati F., Jones T. W., Kang H., Ryu D., 2001, *ApJ*, **562**, 233
- Nelson D., Vogelsberger M., Genel S., Sijacki D., Kereš D., Springel V., Hernquist L., 2013, *MNRAS*, **429**, 3353
- Nelson D., et al., 2015a, *Astronomy and Computing*, **13**, 12
- Nelson D., Genel S., Vogelsberger M., Springel V., Sijacki D., Torrey P., Hernquist L., 2015b, *MNRAS*, **448**, 59
- Nelson D., Genel S., Pillepich A., Vogelsberger M., Springel V., Hernquist L., 2016, *MNRAS*, **460**, 2881
- Nulsen P. E. J., Hambrick D. C., McNamara B. R., Rafferty D., Birzan L., Wise M. W., David L. P., 2005a, *ApJ*, **625**, L9
- Nulsen P. E. J., McNamara B. R., Wise M. W., David L. P., 2005b, *ApJ*, **628**, 629
- Ogrea G. A., Brüggen M., 2013, *MNRAS*, **433**, 1701
- Ogrea G. A., Brüggen M., Röttgering H., Simionescu A., Croston J. H., van Weeren R., Hoeft M., 2013a, *MNRAS*, **429**, 2617
- Ogrea G. A., Brüggen M., van Weeren R. J., Röttgering H., Croston J. H., Hoeft M., 2013b, *MNRAS*, **433**, 812
- Ogrea G. A., Brüggen M., van Weeren R. J., Burgmeier A., Simionescu A., 2014, *MNRAS*, **443**, 2463
- Owers M. S., et al., 2014, *ApJ*, **780**, 163
- Pakmor R., Springel V., Bauer A., Mocz P., Munoz D. J., Ohlmann S. T., Schaal K., Zhu C., 2016, *MNRAS*, **455**, 1134
- Pfrommer C., 2008, *MNRAS*, **385**, 1242
- Pfrommer C., Springel V., Enßlin T. A., Jubelgas M., 2006, *MNRAS*, **367**, 113
- Pfrommer C., Enßlin T. A., Springel V., Jubelgas M., Dolag K., 2007, *MNRAS*, **378**, 385
- Pfrommer C., Enßlin T. A., Springel V., 2008, *MNRAS*, **385**, 1211
- Pfrommer C., Chang P., Broderick A. E., 2012, *ApJ*, **752**, 24
- Pfrommer C., Pakmor R., Schaal K., Simpson C. M., Springel V., 2016, preprint, (arXiv:1604.07399)
- Pinzke A., Pfrommer C., 2010, *MNRAS*, **409**, 449
- Pinzke A., Oh S. P., Pfrommer C., 2013, *MNRAS*, **435**, 1061
- Pinzke A., Oh S. P., Pfrommer C., 2015, preprint, (arXiv:1503.07870)
- Planck Collaboration 2013, *A&A*, **554**, A140
- Planelles S., Quilis V., 2013, *MNRAS*, **428**, 1643
- Quilis V., Ibanez J. M. A., Saez D., 1998, *ApJ*, **502**, 518
- Randall S. W., et al., 2011, *ApJ*, **726**, 86
- Russell H. R., et al., 2011, *MNRAS*, **417**, L1
- Russell H. R., et al., 2014, *MNRAS*, **444**, 629
- Ryu D., Kang H., Hallman E., Jones T. W., 2003, *ApJ*, **593**, 599
- Schaal K., Springel V., 2015, *MNRAS*, **446**, 3992
- Sijacki D., Springel V., Di Matteo T., Hernquist L., 2007, *MNRAS*, **380**, 877
- Sijacki D., Vogelsberger M., Genel S., Springel V., Torrey P., Snyder G. F., Nelson D., Hernquist L., 2015, *MNRAS*, **452**, 575
- Skillman S. W., O’Shea B. W., Hallman E. J., Burns J. O., Norman M. L., 2008, *ApJ*, **689**, 1063
- Skillman S. W., Xu H., Hallman E. J., O’Shea B. W., Burns J. O., Li H., Collins D. C., Norman M. L., 2013, *ApJ*, **765**, 21
- Snyder G. F., et al., 2015, *MNRAS*, **454**, 1886
- Sparre M., et al., 2015, *MNRAS*, **447**, 3548
- Springel V., 2010, *MNRAS*, **401**, 791
- Springel V., Hernquist L., 2003, *MNRAS*, **339**, 289
- Springel V., Di Matteo T., Hernquist L., 2005, *MNRAS*, **361**, 776
- Suresh J., Rubin K. H. R., Kannan R., Werk J. K., Hernquist L., Vogelsberger M., 2015a, preprint, (arXiv:1511.00687)
- Suresh J., Bird S., Vogelsberger M., Genel S., Torrey P., Sijacki D., Springel V., Hernquist L., 2015b, *MNRAS*, **448**, 895
- Torrey P., Vogelsberger M., Genel S., Sijacki D., Springel V., Hernquist L., 2014, *MNRAS*, **438**, 1985
- Torrey P., et al., 2015, *MNRAS*, **454**, 2770
- Vazza F., Brunetti G., Gheller C., 2009a, *MNRAS*, **395**, 1333
- Vazza F., Brunetti G., Kritsuk A., Wagner R., Gheller C., Norman M., 2009b, *A&A*, **504**, 33
- Vazza F., Brunetti G., Gheller C., Brunino R., 2010, *New Astron.*, **15**, 695
- Vazza F., Dolag K., Ryu D., Brunetti G., Gheller C., Kang H., Pfrommer C., 2011, *MNRAS*, **418**, 960
- Vazza F., Brüggen M., Gheller C., 2013, *MNRAS*, **428**, 2366
- Vazza F., Gheller C., Brüggen M., 2014, *MNRAS*, **439**, 2662
- Vazza F., Ferrari C., Bonafede A., Brüggen M., Gheller C., Braun R., Brown S., 2015, *Advancing Astrophysics with the Square Kilometre Array*

- (AASKA14), p. 97
- Vogelsberger M., Sijacki D., Kereš D., Springel V., Hernquist L., 2012, *MNRAS*, **425**, 3024
- Vogelsberger M., Genel S., Sijacki D., Torrey P., Springel V., Hernquist L., 2013, *MNRAS*, **436**, 3031
- Vogelsberger M., Genel S., Sijacki D., Torrey P., Springel V., Hernquist L., 2014a, *MNRAS*, **438**, 3607
- Vogelsberger M., et al., 2014b, *MNRAS*, **444**, 1518
- Vogelsberger M., et al., 2014c, *Nature*, **509**, 177
- Wentzel D. G., 1974, *ARA&A*, **12**, 71
- White S. D. M., Frenk C. S., 1991, *ApJ*, **379**, 52
- White S. D. M., Rees M. J., 1978, *MNRAS*, **183**, 341
- van de Voort F., Schaye J., 2012, *MNRAS*, **423**, 2991

with an even higher resolution would result in shocks at very similar locations and with very similar properties.

The inner accretion shock is also present in the non-radiative run Illustris-NR-2, and is hence unrelated to feedback processes. Remarkably, the inner shock is less spherical in this simulation and consists of two connected bow-shaped shocks pointing in the direction of the filaments. This observation leads us to suggest that the sphericity in the full physics runs originates from cooling physics, as discussed in Section 4.1.

This paper has been typeset from a  $\text{\TeX}/\text{\LaTeX}$  file prepared by the author.

## APPENDIX A: RESOLUTION STUDY

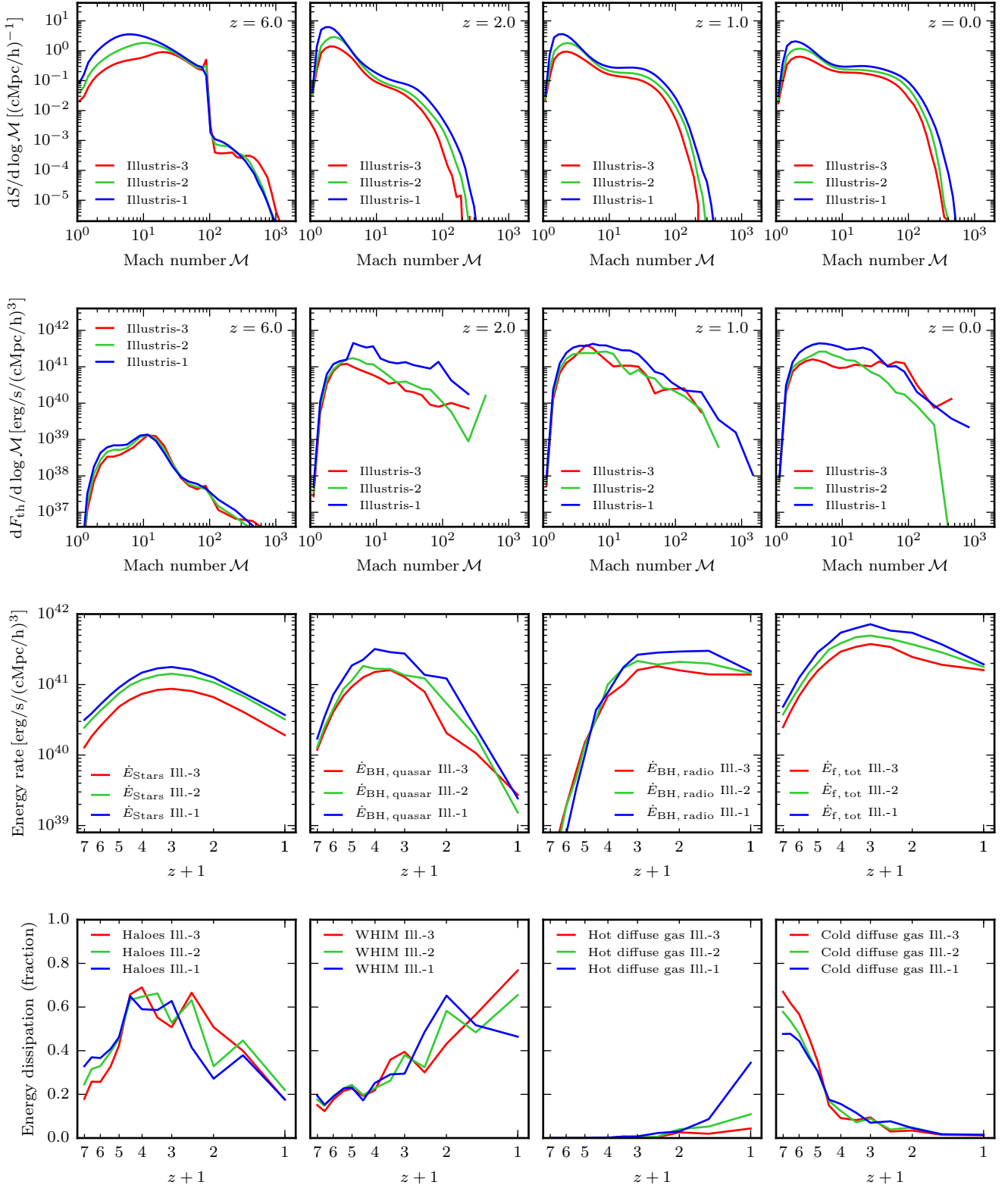
In Fig. A1, we study resolution effects related to shock properties for the full physics runs Illustris-1, Illustris-2, and Illustris-3. Illustris-2 and Illustris-3 have an 8 and 64 times lower mass resolution compared to Illustris-1, respectively, but adopt the same physics model and evolve otherwise identical initial conditions. The first row shows the cumulative shock surface area as a function of Mach number for the different resolutions. The results across cosmic time are similar, with the trend that more shocks are found in higher resolution runs. This is especially true at high redshift. These findings are expected since finer and therefore more numerous structures are resolved with increasing resolution.

In the second row we investigate resolution effects on the energy dissipation at shocks as a function of Mach number. At  $z = 6$  we find very good agreement, indicating that the difference in the cumulative shock surface area at this time is due to less energetic external shocks. At  $z \leq 2$ , shocks with  $\mathcal{M} \gtrsim 5$  dissipate significantly more energy in the highest resolution run compared to Illustris-2 and Illustris-3. As can be seen in the left-hand side panel of Fig. 4, this results in a total energy dissipation which is higher by a factor of around 2 at late times.

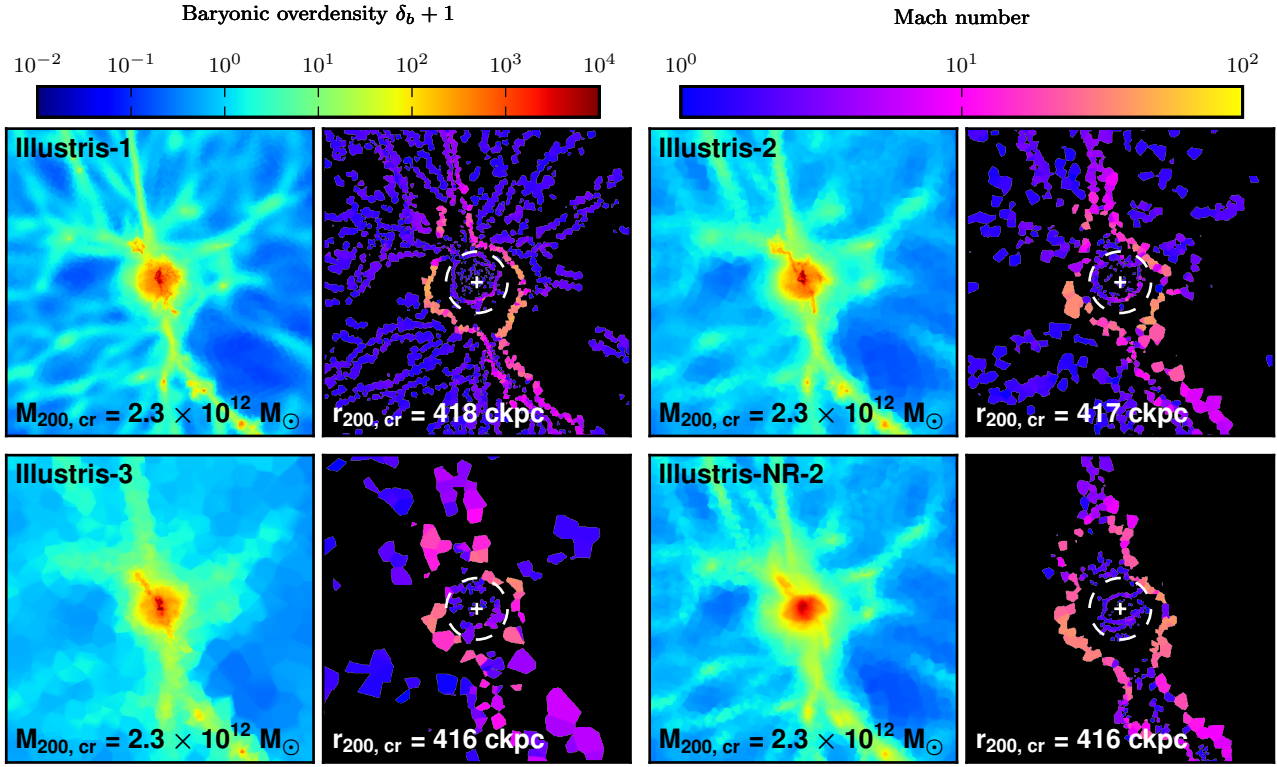
We suspect that the origin of this discrepancy lies in the feedback energy released by BHs, for the following reasons. The energy output of quasar and radio AGN as a function of redshift is shown in the central panels of the third row, and for both channels significantly larger values are reached in the highest resolution run. Moreover, as can be seen in the row at the bottom, a notable hot diffuse phase is only created in Illustris-1. As we have argued in Section 3.2.2, this phase originates from few and highly energetic shocks. Nevertheless, we obtain overall reasonably robust results. Given that the simulations themselves have to produce resolution independent results, as well as the shock finding algorithm, this achievement is non-trivial.

Fig. A2 shows halo 4 of Fig. 7, which can also be seen in the zoom of Fig. 8, for different simulations. It can be seen, as previously discussed, that fewer shocks are found for the lower resolution runs. Moreover, in the non-radiative simulation Illustris-NR-2, many shocks on to the cosmic web are erased by the global temperature floor imposed in post-processing to model reionization. In Illustris-3, the resolution is not high enough for detecting distinct shock surfaces at this scale and redshift ( $z = 4$ ). Nevertheless, the detections at hand point towards the existence of a double accretion shock. On the other hand, in Illustris-1 and Illustris-2, the inner and the outer accretion shock are clearly visible, and moreover, the measured Mach numbers are similar. We hence expect that these surfaces are largely converged; running the simulation





**Figure A1.** Convergence study of several quantities of the full physics runs. From top to bottom we show the cumulative shock surface as a function of Mach number, the energy dissipation at shocks as a function of Mach number, the energy released in different feedback channels as a function of redshift, and the corresponding energy dissipation within different environments as a function of redshift. A higher BH feedback energy rate is present in Illustris-1 compared to the lower resolution runs, and we suspect this to be the main reason for the increased energy dissipation rate at shocks for  $z \leq 2$ .



**Figure A2.** Resolution study for the halo with double accretion shock shown in Fig. 8. Although less details are resolved in the lower resolution runs, the inner accretion shock can still be seen. Moreover, it is also present in the non-radiative run Illustris-NR-2, providing evidence that this shock is truly an accretion phenomenon. In the full physics runs the shape of the inner shock is roughly spherical, whereas in the non-radiative run it consists of connected bow-shaped shocks, suggesting that cooling helps to stabilize the inner accretion shock and make them more spherical.